Chemical Science

ROYAL SOCIETY OF CHEMISTRY

EDGE ARTICLE

View Article Online
View Journal | View Issue

Check for updates

Cite this: *Chem. Sci.*, 2025, **16**, 1932

All publication charges for this article have been paid for by the Royal Society of Chemistry

Open Access Article. Published on 18 December 2024. Downloaded on 2/10/2026 7:04:31 AM. This article is licensed under a Creative Commons Attribution-NonCommercial 3.0 Unported Licence.

Interplay between A-site and oxygen-vacancy ordering, and mixed electron/oxide-ion conductivity in $n = 1$ Ruddlesden–Popper perovskite $Sr_2Nd_2Zn_2O_7$†

Danhe Li,‡[a] Guangxiang Lu,‡[a] Zien Cheng,[a] Maxim Avdeev, *[bc] Jungu Xu, [d] Zhengyang Zhou,[e] Rihong Cong, [a] Tao Yang *[a] and Pengfei Jiang *[a]

Oxygen vacancies in Ruddlesden–Popper (RP) perovskites (PV) $[AO][ABO_3]_n$ play a pivotal role in engineering functional properties and thus understanding the relationship between oxygen-vacancy distribution and physical properties can open up new strategies for fine manipulation of structure-driven functionalities. However, the structural origin of preferential distribution for oxygen vacancies in RP structures is not well understood, notably in the single-layer ($n = 1$) RP-structure. Herein, the $n = 1$ RP phase $Sr_2Nd_2Zn_2O_7$ was rationally designed and structurally characterized by combining three-dimensional (3D) electron diffraction and neutron powder diffraction. $Sr_2Nd_2Zn_2O_7$ adopts a novel 2-fold $n = 1$ RP-type *Pmmn*-superstructure due to the concurrence of A-site column ordering and oxygen-vacancy array ordering. These two ordering models are inextricably linked, and disrupting one would thus destroy the other. Oxygen vacancies are structurally confined to occupy the equatorial sites of "BO_6"-octahedra, in stark contrast to the preferential occupation of the inner apical sites in $n \geq 2$ structures. Such a layer-dependent oxygen-vacancy distribution in RP structures is in fact dictated by the reduction of the cationic A–A/B repulsion. Moreover, the intrinsic oxygen vacancies can capture atmospheric O_2, consequently resulting in a mixed oxide ion and p-type electrical conductivity of 1.0×10^{-4} S cm^{-1} at temperatures > 800 °C. This value could be further enhanced to > 1.0×10^{-3} S cm^{-1} by creating additional oxygen vacancies on the equatorial sites through acceptor doping. Bond valence site energy analysis indicates that the oxide ion conduction in $Sr_2Nd_2Zn_2O_7$ is predominated by the one-dimensional pathways along the $[Zn_2O_7]$ ladders and is triggered by the gate-control-like migration of the equatorial bridging oxygens to the oxygen-vacant sites. Our results demonstrate that control of anion and cation ordering in RP perovskites opens a new path toward innovative structure-driven property design.

Received 8th August 2024
Accepted 14th December 2024

DOI: 10.1039/d4sc05323k

rsc.li/chemical-science

1. Introduction

Ruddlesden–Popper (RP) phases with the general formula $[AO][ABO_3]_n$ are an attractive family of perovskite derivatives due to their low dimensional topology of crystal structure and associated functional properties, such as high-temperature superconductivity,[1,2] room temperature multiferroic,[3] ferroelectric,[4–6] oxide ion conduction,[7,8] and uniaxial negative thermal expansion (NTE),[9–11] and photocatalytic properties.[12,13] The layered RP structure can be viewed as a stacking of $[ABO_3]$ perovskite slabs along the [001] direction with an additional sheet of rock salt [AO] layer interposed every n layers. The perovskite slab is displaced relatively to its neighboring sheets by a vector of [1/2, 1/2, 0], thereby resulting in a body-centered tetragonal structure described by the space group *I*4/*mmm*.

Recently, the tilt engineering toward polar RP perovskite design has been of great interest to chemists because the traditional active distortion center-driven polar structure design using the closed-shell d^0 and s^2 cations encountered failure in the RP perovskite family. Hence, strenuous efforts had been devoted to design NCS double- and single-layer RP perovskites theoretically and experimentally. The trilinear ubiquitous

[a]*College of Chemistry and Chemical Engineering, Chongqing University, Chongqing 401331, China. E-mail: taoyang@cqu.edu.cn; pengfeijiang@cqu.edu.cn*

[b]*Australian Nuclear Science and Technology Organisation, Lucas Height, NSW 2234, Australia. E-mail: max@ansto.gov.au*

[c]*School of Chemistry, The University of Sydney, Sydney, NSW 2006, Australia*

[d]*College of Materials Science and Engineering, Guilin University of Technology, Guilin, Guangxi 541004, China*

[e]*Shanghai Institution of Ceramics, Chinese of Academy of Science, Shanghai 201899, China*

† Electronic supplementary information (ESI) available. See DOI: https://doi.org/10.1039/d4sc05323k

‡ These authors contributed equally to the manuscript.

© 2025 The Author(s). Published by the Royal Society of Chemistry

Open Access Article. Published on 18 December 2024. Downloaded on 2/10/2026 7:04:31 AM. This article is licensed under a Creative Commons Attribution-NonCommercial 3.0 Unported Licence.

octahedral tilting or rotation distortions of $a^-a^-c^+$ for the perovskite slabs have shown as an effective approach to achieving inversion symmetry breaking for double layer ($n = 2$) RP structure through a manipulation of tolerance factor[3–6,10] or topochemical incorporation of fluoride ions into interstitial sites in the rock-salt layers.[14] In a single-layer ($n = 1$) RP structure, simple octahedral tilting and SOJT ordering models are both incapable of breaking the inversion symmetry, however, combining the two with A-site cation ordering allows polar structure formation.[15] This has been observed indeed for NCS $P\bar{4}2_1m$-ALnTiO$_4$ (A = Ag and Na) with layered A/Ln ordering and $a^-b^0c^0/a^0b^-c^0$ octahedral rotation for successive perovskite layers.[16,17] The degree of lattice freedom is plausibly responsible for the difference in structure-driven NCS design strategy between double- and single-layer RP structures. This structure-driven polar RP oxide design removes the reliance on d^0 and s^2 cations to realize ferroelectricity and thus expands the chemical composition space for the rational design of RP-type multiferroics.

Another intriguing feature of the RP structure is the capability of accommodating oxygen defects which are directly correlated to the physical properties. For instance, oxygen vacancies are present in the RP-type superconductor $La_3Ni_2O_{7-\delta}$ and are found to preferentially occupy the inner apical site of the NiO_6-octahedra.[18] The oxygen vacancies can lead to strong charge transfer characteristics for $La_3Ni_2O_{7-\delta}$ and have been proposed to be crucial to high-temperature superconductivity under high-pressure conditions, in particular the suppression of the critical temperature T_c.[19,20] In contrast, the more flexible $n = 1$ RP phases $Ln_2NiO_{4+\delta}$ (Ln = rare earth) allow oxygen hyperstoichiometry in the rock-salt (RS) layer and concurrently partially oxidizes Ni^{2+} into Ni^{3+}, resulting in structural symmetry lowering from prototype *I*4/*mmm* to orthorhombic *Fmmm*.[8] It has been reported that the interstitial oxygen ions in the RS layer are ordered on a sub-mesoscopic scale[21] and could diffuse and exchange with the apical oxygens of NiO_6-octahedra,[22,23] thus giving rise to high oxide ion conductivity at ambient temperature. The significant oxide ion conduction together with the mixed Ni^{2+}/Ni^{3+} valences make $Ln_2NiO_{4+\delta}$ a promising candidate as cathode materials for solid oxide fuel cells (SOFCs).

In this work, we turned our attention to oxygen-deficient $n = 1$ RP structure with mixed A-cations on account of the following reasons: (1) the flexible structure with a high ratio of terminal oxygen ions, as compared to the $n \geq 2$ structures, may give rise to fast ionic conduction; (2) the introduction of oxygen vacancies in the structure could further facilitate the oxygen-vacancy interexchange, thereby enhancing the ionic conductivity; (3) the principle determining oxygen-vacancy distribution has never been well understood in the RP-structure family. In this context, we targeted the hitherto unreported oxygen-deficient $n = 1$ RP phase $Sr_2Nd_2Zn_2O_7$ ($SrNdZnO_{3.5}$), where the A-site Sr^{2+} (1.31 Å for 9-fold coordination) and Nd^{3+} (1.16 Å for 9-fold coordination) cations with distinctive ionic size, charges, and chemical bonding characteristics are conducive to the oxygen-vacancy stabilization in the local scale. Structure solution based on three-dimensional (3D) electron diffraction (ED) and high-resolution neutron powder diffraction data revealed that this novel oxide is the first A-site cation and oxygen vacancy concurrently ordered $n = 1$ RP perovskite. Most importantly, we found that A-site cationic ordering and oxygen-vacancy ordering are coupled, that is, disrupting ordering in one sublattice destroys ordering in the other. The oxygen vacancies in the $n = 1$ RP structure were found to favor the equatorial position of the BO_6-octahedra, in sharp contrast to the apical position preference observed for $n \geq 2$ RP structures. Moreover, $Sr_2Nd_2Zn_2O_7$ is a semiconductor exhibiting mixed oxide ionic and electronic conduction, demonstrating its potential application as SOFC cathode materials.

2. Experimental section

2.1 Synthesis

Polycrystalline samples of $Sr_2Nd_2Zn_2O_7$ were prepared by the conventional solid-state reaction method using high purity $SrCO_3$ (99.99%, Alfa Aesar), Nd_2O_3 (99.99%, Beijing Founde Star Science & Technology Co., Ltd) and ZnO (99.99%, Sichuan High-Purity Material Technology Co., Ltd) powders as starting materials. A stoichiometric amount of these raw materials was weighed and mixed thoroughly in an agate mortar and then preheated at 900 °C for 10 h. The resulting powders were further ground and pelletized and then calcinated at 1100 °C with a dwell time of 40 h with intermediate regrinding and pelleting. The compositions $Sr_2Nd_{2-x}La_xZn_2O_7$ (x = 0.5, 1, 1.5, and 2), $Sr_2Nd_2Zn_{2-y}In_yO_{7+y/2}$ (y = 0.06, 0.1, 0.14, 0.2), and $Sr_{2.1}Nd_{1.9}Zn_2O_{6.95}$ were prepared using the same procedure described above.

2.2 Characterization

The phase formation and purity of samples were assessed by powder X-ray diffraction (PXRD) using a laboratory PANalytical Empyrean Alpha-1 diffractometer (Cu $K_{\alpha 1}$ radiation) equipped with a Johansson Ge(111) monochromator. High-resolution PXRD used for Rietveld refinements were collected in the 2θ-range of 10–120° with a step size of 0.00656° and a counting time of 900 s. Constant-wavelength neutron powder diffraction (NPD) data for $Sr_2Nd_2Zn_2O_7$ and $Sr_2La_2Zn_2O_7$ were collected on the high-resolution ECHIDNA powder diffractometer at OPAL research facility (Lucas Height, Australia) with a step size of 0.05° and a wavelength of 1.6220 Å.[24] The lattice parameters of $Sr_2Nd_2Zn_2O_7$ were obtained by indexing the PXRD pattern using the LP-search method implemented in Academic Topas V7 software.[25,26] Combined Rietveld refinements against both PXRD and NPD were also performed with the Academic Topas V7 software.

Powder samples of $Sr_2Nd_2Zn_2O_7$ were ground thoroughly and transferred into a test tube with 2 mL absolute ethanol. After ultrasonic treatment for 10 min, 2 drops of the suspension were deposited on a carbon film-coated copper grid and then dried for 5 min before transmission electron microscope (TEM) and scanning electron microscope (SEM) measurements. The precession electron diffraction tomography (PEDT) three-dimensional (3D) electron diffraction (ED) data were collected

Open Access Article. Published on 18 December 2024. Downloaded on 2/10/2026 7:04:31 AM. This article is licensed under a Creative Commons Attribution-NonCommercial 3.0 Unported Licence.

on the FEI Tecnai G2 F20 TEM (200 eV) equipped with a Gatan 321 camera. The precession speed was 100 Hz, and the exposure time of every frame was 2 s. PEDT data reduction was performed with the software PETS version 2.0.[27]

The elemental analyses were performed using energy-dispersive X-ray spectroscopy in a Talos F200s G2 TEM. X-ray photoelectric spectroscopy (XPS) measurements were performed on the Thermo Fisher Scientific ESCALAB 250Xi X-ray photoelectron spectrometer with a monochromatic Al Kα X-ray beam source. The binding energies were calibrated according to the C 1s peak energy of 284.5 eV. The ultraviolet-visible (UV-vis) light diffuse spectra for $Sr_2Nd_2Zn_2O_7$ were measured from 200 to 1200 nm using a Shimadzu UV-3600 spectrometer. Fine powders were spread on the surface of compressed $BaSO_4$ as a 100% reflectance standard.

The electronic transport properties of $Sr_2Nd_2Zn_2O_7$ were investigated by using a Solartron 1260A impedance phase analyzer in the frequency range of 10^{-1}–10^{7} Hz with an applied oscillation voltage of 100 mV. The disk-shaped pellets with > 90% relative density were used for AC impedance spectroscopy measurements over the temperature range from 300 to 1000 °C under various atmospheres. Before the measurements, the flat parallel surfaces of the pellet were coated with Pt paste and calcinated at 800 °C for one hour in air to form metal electrodes and ensure good contact between the pellet and electrodes. The oxygen transport number was determined by measuring the electromotive force (EMF) of the ceramic pellet of $Sr_2Nd_2Zn_2O_7$ using the oxygen concentration cell method over the temperature range of 500–800 °C. The pellet was attached to an alumina tube with a glass adhesive seal. One side of the pellet was exposed to 2% O_2 in Ar flow and the other side was exposed to pure O_2 flow (1 atm).

2.3 Theoretical calculations

First principles density functional theory (DFT) calculations were carried out using the projector augmented wave (PAW) method implemented in the Vienna *ab initio* Simulation Package (VASP).[28] The generalized gradient approximation (GGA) parametrized by Perdew, Burke, and Ernzerhof was employed to describe the exchange–correlation potential.[29,30] The cutoff energy of the plane basis was set at 520 eV, and the lattice parameters and atomic positions were optimized until the residual force was less than 0.01 eV $Å^{-1}$. The convergence criterion for electronic self-interactions was the change of the total energy within 10^{-6} eV. A 2 × 7 × 3 *k*-space mesh was employed to sample the Brillouin zone. We should emphasize that a completely ordered $Sr_2Nd_2Zn_2O_7$ model was used for DFT calculations.

3. Results and discussion

3.1 Crystal structure determination

The combination of Sr, Nd, and Zn cations in a 1 : 1 : 1 ratio leads to the formation of the hitherto unreported new oxide $Sr_2Nd_2Zn_2O_7$. Complementary elemental analysis using TEM-EDS further confirms that the cationic ratio of Sr : Nd : Zn is in line with the nominal chemical composition within expected errors and no elemental aggregation was detected (Fig. S1†), confirming the single phase of $Sr_2Nd_2Zn_2O_7$. High-resolution XPS signals for Sr 3d, Nd 3d, and Zn 2p demonstrate that these elements take valence states of +2, +3, and +2, respectively (Fig. S2†). Compared to the PXRD of archetype $n = 1$ RP-perovskite, the PXRD pattern of $Sr_2Nd_2Zn_2O_7$ is much more complicated with the splitting of the main diffraction peaks and a series of additional sharp peaks (Fig. S3†), plausibly ascribed to either the A-site cationic order, the oxygen-vacancy ordering, or the combination of both. Indexing of the PXRD pattern of $Sr_2Nd_2Zn_2O_7$ resulted in a primitive orthorhombic unit cell with lattice parameters of $a \approx 13.23$, $b \approx 3.71$, and $c \approx 7.51$ Å. Such a lattice is in correspondences with a 2-fold $n = 1$ RP-superstructure with $a = c_t$, $b = a_t$, $c = 2a_t$, where a_t and c_t are the lattice parameters of archetype $n = 1$ RP perovskite described by space group *I*4/*mmm*. Further inspection of the reflection conditions revealed $h00$ for $h = 2n$, $0k0$ for $k = 2n$, and $h + k = 2n$ for $hk0$, indicative of two possible space groups, *Pmmn* (no. 59) and $Pm2_1n$ (no. 31). The lattice dimensions as well as the reflection conditions for $Sr_2Nd_2Zn_2O_7$ were also validated by our 3D ED presented in Fig. 1a–c. To confirm the structural symmetry, we measured the optical second-harmonic generation (SHG), which is a powerful tool to probe the inversion symmetry breaking for a material. The absence of SHG signal suggests the centrosymmetric *Pmmn*-symmetry for $Sr_2Nd_2Zn_2O_7$.

We then used the web-based tool ISODISTORT to generate the initial *Pmmn* model using an archetype $n = 1$ RP-structure (*I*4/*mmm*) as an input model.[31,32] The resulting *Pmmn* model contains two A-sites (two 4f sites), two B-sites (two 2a sites), and six oxygen sites (two 2a, two 2b, and two 4f sites), allowing both A-site cationic ordering and oxygen-vacancy ordering. Owing to the presence of heavy cations like Nd^{3+} in $Sr_2Nd_2Zn_2O_7$, X-ray diffraction is not very sensitive to distribution of oxygen vacancies and we thus collected high-resolution NPD to gain an insight into the possible oxygen vacancy ordering as well as A-site cationic ordering. Consequently, the site occupancy factors (sof.) of the six independent oxygen sites were refined freely and the Sr/Nd distribution over the two A-sites was allowed to vary with the constraints that each site is fully occupied and the overall ratio of Sr/Nd is constrained to be 1 : 1 during the preliminary Rietveld refinement process. The combined Rietveld refinements against both PXRD and NPD data converged smoothly and manifested that the sof. value for one 2a oxygen site converged to zero, whereas those of the remaining five oxygen sites are near unity, firmly evidencing oxygen-vacancy ordering. Hence, during the final refinement stage, the sof. values for the five oxygen sites were fixed to unity and constraints were still applied to sof. values for the A-site Sr^{2+} and Nd^{3+} cations, yielding reliable overall residual factors of $R_{wp} = 3.27\%$, $R_p = 2.41\%$, and $\chi^2 = 1.86$. The final Rietveld refinement patterns are exemplified in Fig. 1d and e. The final crystallographic data, atomic coordinates, sof. values, isotropic thermal displacement factors, and interatomic bond distances are listed in Tables 1, 2 and S1.† This oxygen-vacancy ordered

© 2025 The Author(s). Published by the Royal Society of Chemistry

Open Access Article. Published on 18 December 2024. Downloaded on 2/10/2026 7:04:31 AM. This article is licensed under a Creative Commons Attribution-NonCommercial 3.0 Unported Licence.

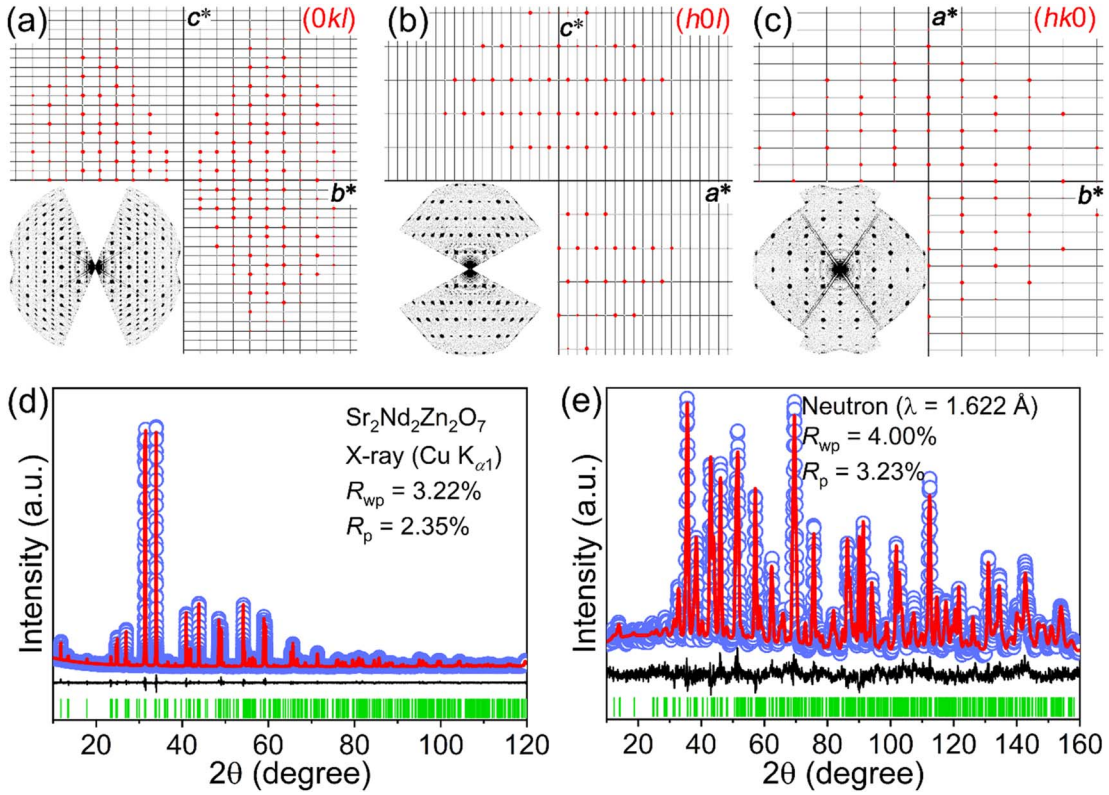

Fig. 1 (a–c) Reconstructed diffraction patterns for the 0*kl*, *h*0*l*, and *hk*0 diffraction planes based on the 3D electron diffraction data. Rietveld refinement plots of high-resolution NPD (d) and PXRD (e) data for $Sr_2Nd_2Zn_2O_7$. Light blue circles, red and black solid lines indicate the observed data, calculated data, and their difference, respectively. The expected Bragg reflections are shown as green bars at the bottom of the patterns.

Table 1 Crystallographic data for $Sr_2Nd_2Zn_2O_7$ obtained from combined Rietveld refinements

Formula	$Sr_2Nd_2Zn_2O_7$	
Source	X-ray (Cu $K_{\alpha1}$)	Neutron
Temperature (K)	298	
Wavelength (Å)	1.5406	1.622
Space group (no.)	*Pmmn* (no. 59)	
a (Å)	13.2291(4)	
b (Å)	3.7145(2)	
c (Å)	7.5085(4)	
V (Å^3)	368.98(4)	
Z	2	
d-Spacing (Å)	0.82–11	0.82–10
R_{wp} (%)	4.00	3.22
R_p (%)	3.23	2.35
R_{exp} (%)	2.43	2.82
χ^2	1.93	1.42

Table 2 Atomic coordinates, sof. values, isotropic thermal displacement factors of $Sr_2Nd_2Zn_2O_7$ obtained from combined Rietveld refinement against both X-ray and neutron powder diffraction data

Atom	Site	*x*	*y*	*z*	sof.	B_{iso} (Å^2)
Sr1/Nd	4f	0.35803(7)	0	0.3704(3)	0.846(2)/0.154(2)	0.75(3)
Nd1/Sr	4f	0.34975(6)	0	0.8724(2)	0.846(2)/0.154(2)	0.43(2)
Zn1	2a	0	0	0.8812(6)	1	1.1(2)
Zn2	2a	0	0	0.3738(7)	1	0.6(1)
O1	2b	0	0.5	0.960(2)	1	1.4(2)
O2	2a	0	0	0.645(2)	1	1.5(2)
O3	2b	0	0.5	0.322(2)	1	0.3(1)
O4	4f	0.1675(6)	0	0.896(2)	1	0.4(1)
O5	4f	0.1758(5)	0	0.3459(9)	1	1.0(1)

model was also validated by our *ab initio* structure solution using the 3D ED data.

3.2 Crystal structure of $Sr_2Nd_2Zn_2O_7$

Fig. 2a shows an ideal $n = 1$ RP perovskite (PV) structure A_2BO_4, which is constructed by a succession of rock-salt (RS) AO layers separated by BO_2 sheets in the sequence of –[AO–AO–BO_2]–. The layered $n = 1$ RP perovskite could also be described as an intergrowth of the RS AO layer with a single ABO_3 perovskite layer, thereby giving the general formula of [AO][ABO_3]. As shown in Fig. 2b, $Sr_2Nd_2Zn_2O_7$ adopts an oxygen-deficient RP perovskite structure ($n = 1$) with the oxygen vacancies (□) exclusively located at the "ZnO_2" layers, resulting in a stacking sequence of –[$Sr_{0.5}Nd_{0.5}O$–$Sr_{0.5}Nd_{0.5}O$–$ZnO_{1.5}$]–. The oxygen vacancies are ordered by removing every other oxygen-only column in the ZnO_2 layer, thereby doubling the *c*-axis and thus forming the first oxygen-deficient 2-fold $n = 1$ RP superstructure. Such an oxygen vacancy ordering converts the octahedrally coordinated B-site cations in [AO][ABO_3] into ZnO_5 square pyramids for all crystallographically independent Zn^{2+}

Open Access Article. Published on 18 December 2024. Downloaded on 2/10/2026 7:04:31 AM.
This article is licensed under a Creative Commons Attribution-NonCommercial 3.0 Unported Licence.

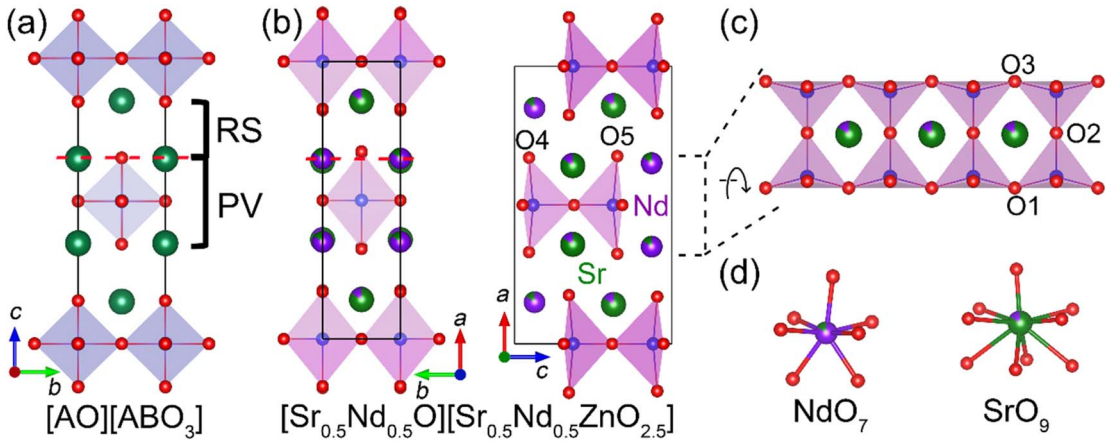

Fig. 2 Structural comparison of aristotype $n = 1$ RP structure $[AO][ABO_3]$ (a) and oxygen-deficient $Sr_2Nd_2Zn_2O_7$ (b). The one-dimensional Zn_2O_7 ladder (c) and the coordination environments of the A-site Sr^{2+}/Nd^{3+} cations (d) in $Sr_2Nd_2Zn_2O_7$.

cations in $Sr_2Nd_2Zn_2O_7$ and, more importantly, transforms the two-dimensional (2D) perovskite slabs into one dimensional (1D) ladder-like Zn_2O_7 chains parallel with the *c*-axis. This 1D Zn_2O_7 ladder built by ZnO_5 square pyramids *via* vertex-sharing has never been reported for perovskite-related structures to the best of the authors' knowledge. Moreover, the oxygen vacancy ordering also leads to one-half of A-site cations maintaining 9-fold coordination, whereas the other half is reduced to a 7-fold coordination (see Fig. 2d). Owing to the relatively large contrast in ionic radius ($\Delta r = 0.147$ Å) between Sr^{2+} (1.31 Å for 9-fold coordination) and Nd^{3+} (1.163 Å for 9-fold coordination),[33] there should be a tendency for the smaller Nd^{3+} to preferentially reside on the 7-coordinated A-site. This inference agrees with the fact that a large long-range order (LRO) parameter of 69.2% was obtained for A-site Sr^{2+}/Nd^{3+} cations according to the Rietveld refinement results (Table 2) and the equation $LRO = (2 \times S) - 1$, where S is the predominate site occupation factor of the A-site. In terms of structure, the A-site Sr^{2+}/Nd^{3+} cations are partially column-ordered in the RS layers along the $[100]_p$ direction, where the subscript index p represents the ideal cubic ABO_3 perovskite. Altogether, according to the A-cationic ordering and oxygen vacancy distribution, the chemical formula of $Sr_2Nd_2Zn_2O_7$ could be written as $[Sr_{0.5}Nd_{0.5}O][Sr_{0.5}Nd_{0.5}ZnO_{2.5}]$.

To stabilize the oxygen vacancy ordering and A-site cationic ordering, synergetic atomic displacement is required to release the lattice strain, thereby resulting in a significant structural distortion as compared to the archetype $n = 1$ RP PV structure. To quantitatively analyze this structural distortion, the atomic positional displacements in $Sr_2Nd_2Zn_2O_7$ were calculated with respect to those in an idealized $n = 1$ RP PV structure with the same lattice matrix. As shown in Fig. 3, the displacements for the cations and O2 anion are negligible (< 0.1 Å), as compared to the remaining oxygen ions (O1, O3, O4, and O5) located at the basal plane of the ZnO_5 square pyramid with large displacements > 0.3 Å. The large displacements of O4 and O5 ions toward the adjacent RS layer and intralayer Nd^{3+} cations lead to a significant rumpling of the RS layer, manifested by the significant protrusion of oxygens from the $[Sr_{0.5}Nd_{0.5}]_{RS}$ cationic sublayer (see Fig. 2b). Such a protrusion of oxygen ions is usually negligible in RP PV with neutron $[A^{2+}O]$ layers. Hence, the rumpling of the RS layer in $Sr_2Nd_2Zn_2O_7$ should be a result of the coordination requirement of the smaller Nd^{3+} and positively charged $[Sr_{0.5}Nd_{0.5}O]^{0.5+}$ RS layer. The rumpling of the RS layer also leads to the deformation of the ZnO_5 square pyramids, reflected by remarkably long Zn–O4/O5 bond lengths. As shown in Table S1,† the Zn1–O4 and Zn2–O5 bond lengths of 2.258(6) and 2.334(7) Å, respectively, are significantly longer than the remaining Zn–O bonds (< 2.0 Å) and are also much larger than the expected Zn–O bond length of 2.06 Å estimated from the sum of the ionic radii for Zn^{2+} (0.68 Å) and O^{2-} (1.38 Å), resulting in large distortion indexes of 0.075 and 0.102 for $Zn1O_5$ and $Zn2O_5$ square pyramids, respectively, from the aspect of bond length. In this context, the O1 and O3 ions are forced to displace within the oxygen-deficient $ZnO_{1.5}$ sublayer to satisfy the bonding requirement of Zn^{2+}, thereby causing

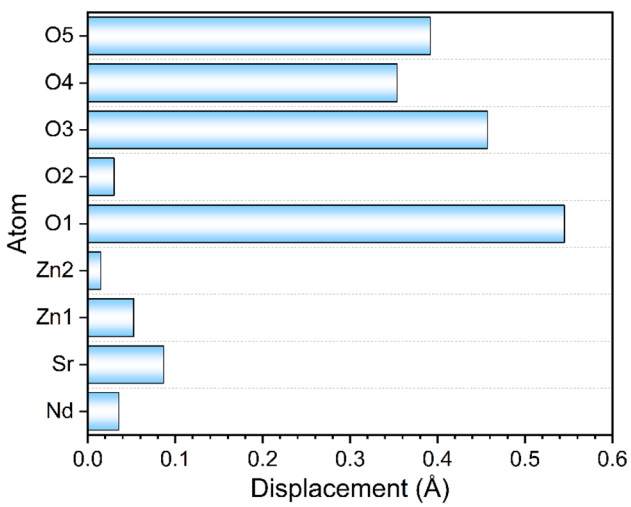

Fig. 3 Atomic displacements in $Sr_2Nd_2Zn_2O_7$ with respect to those in the archetype $n = 1$ RP perovskite.

© 2025 The Author(s). Published by the Royal Society of Chemistry

Open Access Article. Published on 18 December 2024. Downloaded on 2/10/2026 7:04:31 AM. This article is licensed under a Creative Commons Attribution-NonCommercial 3.0 Unported Licence.

a compressed basal plane along the *b*-axis for the ZnO_5 square pyramids (see Fig. 2b). These positional displacements for oxygen anions create perfect coordination environments for Zn1 and Zn2 cations with bond valence sum (BVS) values of 1.99 and 2.05, respectively.[34] In contrast, both Sr^{2+} (BVS = 1.59) and Nd^{3+} (BVS = 2.59) are slightly underbonded but are in line with the more ionic bonding character of Sr/Nd–O bonds compared to the covalent Zn–O bonds.

3.3 A-site cation ordering and interplay with oxygen vacancy ordering

For RP perovskites with $n \geq 2$, there are distinct A-sites with different coordination geometries, that is, the 12-fold coordinated A-sites within the PV blocks and the 9-fold coordinated A-sites within the RS slabs. Consequently, layered A-site ordering could be readily achieved in mixed A-cation RP phases ($n \geq 2$) by enlarging the ionic radius differences (ΔIR) between different A-site cations because larger A-cations are prone to occupy the 12-coordinated sites, while smaller A-cations favor the 9-coordinated sites. This has been observed indeed in $n = 2$ RP PVs $Ln_2AB_2O_7$ (Ln = rare earth; A = Ba^{2+} and Sr^{2+}; B = Mn^{3+}, Co^{3+}, Fe^{3+}), where the A-site cationic ordering degree depends on the ΔIR value between Ln^{3+} and A^{2+} cations, that is, a larger ΔIR value will lead to a higher degree of A-site ordering (see Fig. 4a).[35–37] However, as for $n = 1$ RP PV structure, all the A-sites are equivalently possessing a 9-fold coordination environment and long-range A-site cationic ordering is thus improbable. To date, A-site cationic ordering was only reported for $Sr_2La_2LiRuO_8$ (ref. 38) and (Na/K/Ag)$LaTiO_4$ (ref. 16 and 17) (see Fig. 4b and c). For the former, the A-site La^{3+}/Sr^{2+} ordering is a result of 1 : 1 B-site ordering, which creates two crystallographically independent A-sites with distinct sizes and thus results in site-selective 1 : 1 occupation for the La^{3+} and Sr^{2+} cations despite the ΔIR (ΔIR = 0.094 Å) value being relatively small. Moreover, we noticed that La^{3+}/Sr^{2+} cations present column-ordering along the $[110]_p$ direction, dissimilar to the $[100]_p$-directional column-ordering observed in $Sr_2Nd_2Zn_2O_7$. As for (Na/K)$LaTiO_4$, the A-site layered ordering is driven by the large charge difference ($\Delta Q = 2$). Herein, $Sr_2Nd_2Zn_2O_7$ is a unique example that the A-site cationic ordering is associated with oxygen vacancy ordering, which will be discussed in detail latter.

According to the above discussion, the question of whether the large A-site cationic radius difference is essential for stabilizing the unique structure of $Sr_2Nd_2Zn_2O_7$ will arise naturally. To unveil the correlation between A-site cation ordering and oxygen-vacancy ordering hidden in structure, we attempted to synthesize a full solid solution $Sr_2Nd_{2-x}La_xZn_2O_7$ (x = 0.5, 1, 1.5, and 2). As shown in Fig. 5a, the compositions with x = 0.5–2.0 are phase pure and their PXRD patterns could be fitted perfectly using lattice dimensions for a pristine $n = 1$ structure described by space group *I*4/*mmm*, indicative of loss of long-range orderings for both A-site cations and oxygen vacancies. A phase separation was observed for the intermediate composition $Sr_2Nd_{1.75}La_{0.25}Zn_2O_7$, composed of the ordered $Sr_2Nd_2Zn_2O_7$-like *Pmmn*-phases and disordered *I*4/*mmm*-phases. This phase evolution behavior for $Sr_2Nd_{2-x}La_xZn_2O_7$ can be rationalized by observing that partial substitution of Nd^{3+} by the larger La^{3+} makes the average size of Ln^{3+} (Ln = Nd^{3+}, La^{3+}) cation larger, and thus more similar to the size of Sr^{2+}, thereby

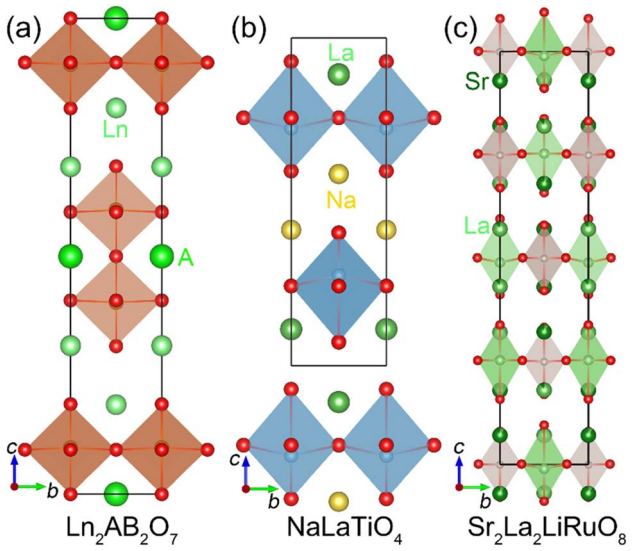

Fig. 4 Crystal structures for A-site cation ordered RP perovskites Ln_2ABO_7 ($n = 2$) (a), $NaLaTiO_4$ ($n = 1$) (b), and $Sr_2La_2LiRuO_8$ ($n = 1$) (c).

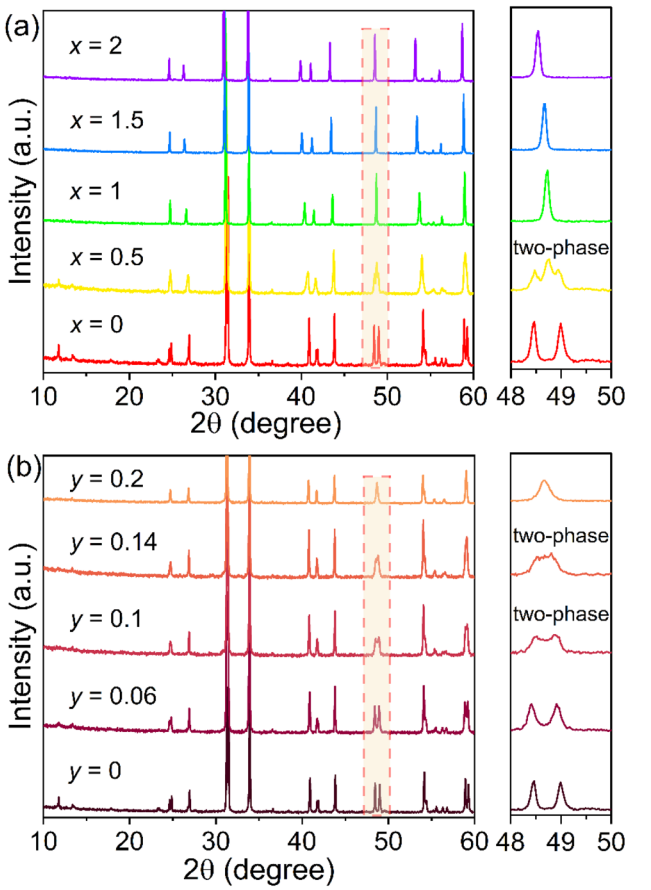

Fig. 5 PXRD patterns for $Sr_2Nd_{2-x}La_xZn_2O_7$ (a) and $Sr_2Nd_2Zn_{2-y}In_yO_{7+y/2}$ (b). The right panels show an enlargement of the light orange regions in PXRD patterns.

Open Access Article. Published on 18 December 2024. Downloaded on 2/10/2026 7:04:31 AM. This article is licensed under a Creative Commons Attribution-NonCommercial 3.0 Unported Licence.

disrupting the A-cation ordering of the host structure and resulting in multiphase behavior. This result indicates that the large size difference between Nd^{3+} and Sr^{2+} is critical to stabilizing the A-site cation as well as the oxygen vacancy ordering in $Sr_2Nd_2Zn_2O_7$.

Conversely, we further investigated the impact of oxygen vacancy disordering on A-site cation ordering by maintaining the ΔIR value for the A-site cations and simultaneously introducing interstitial oxygen ions *via* aliovalent In^{3+}-to-Ga^{3+} substitution in $Sr_2Nd_2Zn_{2-y}In_yO_{7+y/2}$ (y = 0.06, 0.1, 0.14, and 0.2) to disrupt the long-range oxygen vacancy ordering. As shown in Fig. 5b, a biphasic region, where ordered *Pmmn*-structure and disordered *I*4/*mmm*-structure coexist, was also observed for $Sr_2Nd_2Zn_{2-y}In_yO_{7+y/2}$, implying that a small amount of interstitial oxygen ion on the oxygen-vacant sites disrupt the long-range oxygen vacancy ordering and subsequently lead to loss of A-site ordering and thus phase separation. Together with phase formation behavior observed for $Sr_2Nd_{2-x}La_xZn_2O_7$, we can confidently conclude that the A-site ordering is in fact strongly coupled with the oxygen vacancy ordering in $Sr_2Nd_2Zn_2O_7$ and both are indispensable for stabilizing its unique structure. Hence, $Sr_2Nd_2Zn_2O_7$ provides us with a strategy to design A-site ordered n = 1 RP perovskite structures by combining oxygen vacancy order. This strategy perhaps could be expanded to oxygen-deficient $n \geq 2$ RP perovskites, thereby resulting in various A-cation ordering patterns in addition to the commonly observed A-site layered ordering.

3.4 Oxygen-vacancy and anion ordering in RP PV

Another intriguing structural feature of $Sr_2La_2Zn_2O_7$ is the presence of oxygen-vacancy arrays, which are exclusively located at the equatorial positions of the $ZnO_5\square$-octahedra. Oxygen-vacancy array ordering has also been observed in n = 1 RP perovskite derivatives A_2BO_3 (A = La/Sr, B = Cu/Fe/Co/Ir) that exhibit a higher count of oxygen vacancies.[39–41] Most of these compounds were synthesized by the topochemical removal of all oxygen-only columns within the "BO_2" layers, thereby resulting in the formation of infinite 1D chains of apex-linked BO_4 squares (See Fig. 6a). $LaSrCuO_{3.5}$ and $A_2MnO_{3.5}$ (A = Sr and Ca), with an identical oxygen-content to $Sr_2La_2Zn_2O_7$, exhibit a more complex ordering manner of oxygen vacancies, characterized by oxygen vacancies presented in both "BO"- and oxygen-only-columns and absence of oxygen-vacancy arrays.[42–44] Consequently, $LaSrCuO_{3.5}$ and $A_2MnO_{3.5}$ are both composed of infinite 2D infinite layers. The former features a complex (3 + 2) D modulated structure comprising infinite 2D layers composed of mixed CuO_4, CuO_5 and CuO_6 coordinate geometries,[42] whereas the latter is merely consisted of interconnected MnO_5 square pyramids (see Fig. S4†).[43,44] A common structural feature among these oxygen-deficient n = 1 RP perovskites is that the oxygen vacancies are exclusively located at the equatorial positions of the "BO_6"-octahedra.

For oxygen-deficient n = 2 RP perovskites, the oxygen vacancies predominantly occupy the inner apical position of the BO_6-octahedra within the perovskite layer, regardless of whether the oxygen vacancies are ordered. Typical such structures for oxygen-vacancy ordered $Ba_3In_2O_6$ (ref. 45) and disordered $LaSr_2CuTiO_{6.5}$ (ref. 46) are shown in Fig. 6b and c. Our comprehensive structural analyses revealed that this layer-dependent difference in oxygen vacancy distributions is in fact related to the significant change in the coordination environment for the A-site cations caused by oxygen vacancies. Specifically, removing the inner apical oxygen of BO_6 in the n = 2 structure creates a symmetric cubic AO_8 coordination environment for the A-site cations (see Fig. 6d) and maintains their face-sharing connectivity, whereas removal of the equatorial oxygen would lead to an asymmetric AO_7 coordination environment as observed in $Sr_2Nd_2Zn_2O_7$, and transform connection from face-sharing to edge-sharing. In this stage, the apical oxygen vacancy would be energetically favorable and more stable than the equatorial vacancy because the more symmetric face-sharing connectivity can effectively shield the A–A electrostatic repulsion. Consequently, oxygen vacancies favor the apical position in the perovskite layer for the n = 2 structure, which should be also applicable to RP structures with n > 2. More importantly, the removal of the apical oxygen in the RS layer will lead to an extremely asymmetric coordination environment for the A-cation and create A–A/B contacts, thereby

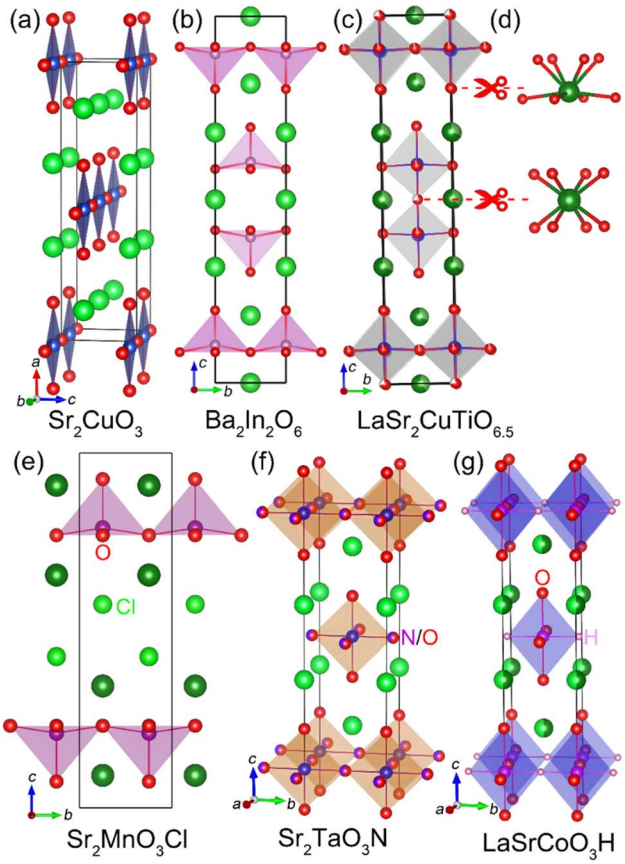

Fig. 6 Crystal structures for oxygen-deficient RP perovskites Sr_2CuO_3 (a), Ba3In2O6 (b), and $LaSr_2CuTiO_{6.5}$ (c). (d) The coordination environment of the A-site cation in n = 2 RP structure after removing different oxygen ions. Anionic ordering in n = 1 RP perovskites Sr_2MnO_3Cl (e), Sr_2TaO_3N (f), and $LaSrCoO_3H$ (g).

© 2025 The Author(s). Published by the Royal Society of Chemistry

Open Access Article. Published on 18 December 2024. Downloaded on 2/10/2026 7:04:31 AM. This article is licensed under a Creative Commons Attribution-NonCommercial 3.0 Unported Licence.

destabilizing the structure. As a result, outer apical oxygen vacancies should be prohibited in RP structures and accordingly, oxygen vacancies should be only allowed in the "BO_2" sublayer of the $n = 1$ RP structure. This conclusion is further consolidated by our Rietveld refinement results for the oxygen vacancy disordered *I*4/*mmm*-$Sr_2La_2Zn_2O_7$ (see Fig. S5, Tables S2 and S3†), where oxygen vacancies are located expectedly at the equatorial positions of the "ZnO_6"-octahedra. Therefore, it is reasonable to assume that long-range A-site and oxygen vacancy disordered $n = 1$ RP PV structure should adopt a $Sr_2Nd_2Zn_2O_7$-like ordered structure on the nanoscale, although this remains to be confirmed by using the neutron pair distribution function analysis.

In addition to oxygen-vacancy ordering, anionic ordering is also readily accessible in $n = 1$ RP perovskite-type mixed anion compounds, such as Sr_2MO_3X (M = V, Mn, Fe, Co, Ni; X = F and Cl) oxyhalides,[47–51] $A_2(Ta/Nb)O_3N$ (A = Ba, Sr, and rare earth) oxynitrides,[52,53] and A_2MO_3H (A = La/Sr/Ba, M = V, Mn, Co, and Li) oxyhydrides.[54–59] In these compounds, Cl^-/F^- and N^{3-} anions preferentially occupy the apical and equatorial sites of the octahedra, respectively (see Fig. 6e and f). These site-selective substitutions in oxyhalides and oxynitrides align with the Pauling's second crystal rule,[53,60] which posits that the electric charge of each anion tends to balance the strength of the electrostatic valence bonds contributed by the cations. Similarly, the hydride anions in A_2MO_3H also preferentially occupy the equatorial sites of the octahedra (see Fig. 6g).[54–59] Additionally, the high mobility of the hydride ions can give rise to significant hydride ion conduction. For instance, La_2LiO_3H exhibits a hydride ion conductivity of 4.6×10^{-6} S cm^{-1} at 280 °C, associated with a relatively high activation energy of 0.72 eV.[59]

3.5 Electronic structure and optical property

The UV-vis absorption spectra of $Nd_2Sr_2Zn_2O_7$ are shown in Fig. 7a, where the absorption edge is at around 380 nm and the absorption peaks in the range of 350–950 nm are attributed to the inner 4f transitions of Nd^{3+}. The absorption spectra were further transformed using the Kubelka–Munk equation to obtain the accurate band gap value (E_g).[61,62] By plotting $(\alpha h\nu)^2$ as a function of $h\nu$ (α is the absorption coefficient, h is the Planck

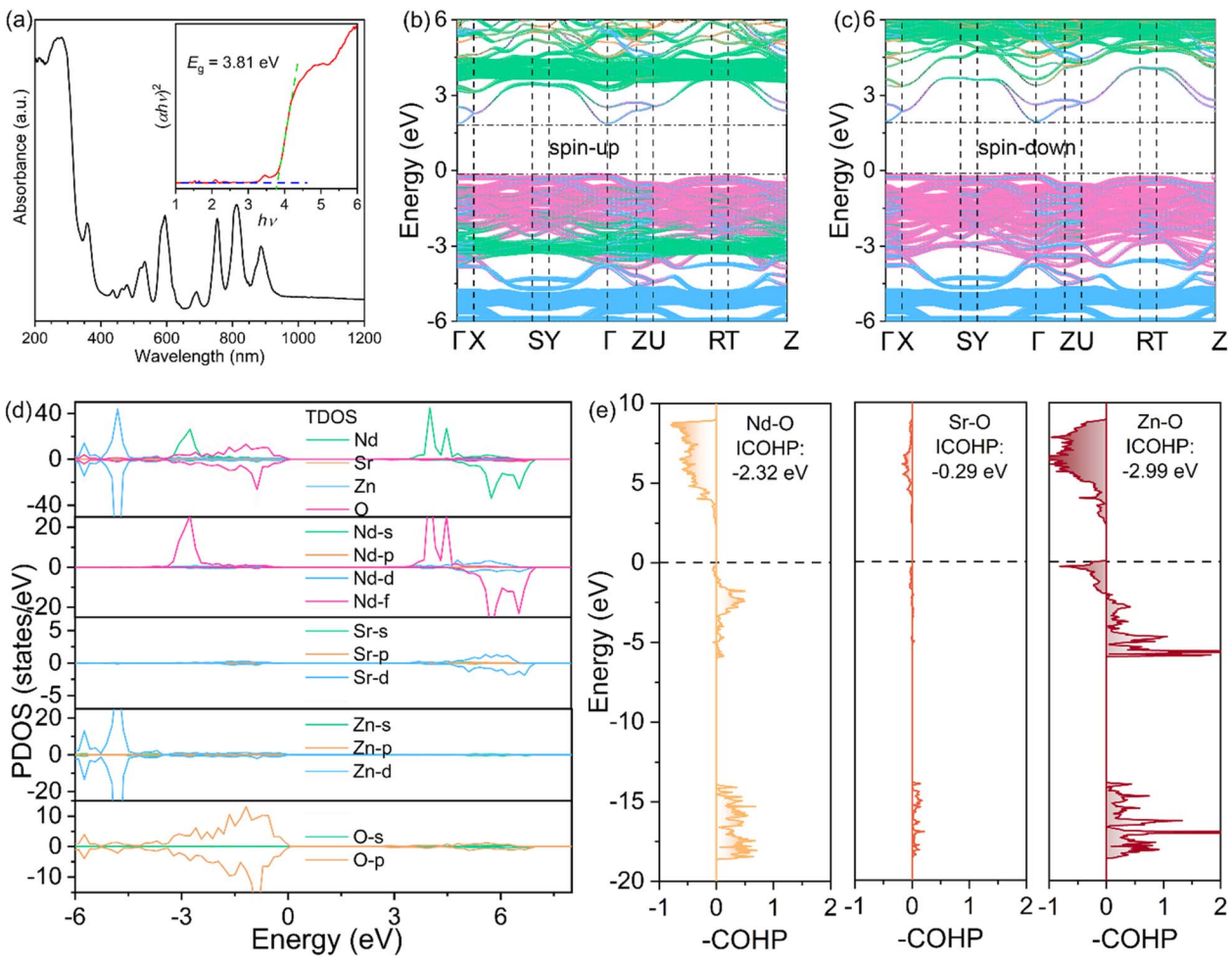

Fig. 7 (a) UV-vis diffusion spectra for $Sr_2Nd_2Zn_2O_7$. The insets show the plots of $(\alpha h\nu)^2$ as a function of phonon energy. (b) Spin-up and (c) spin-down state electronic band structures for $Sr_2Nd_2Zn_2O_7$. (d) Partial density of states for Nd, Sr, Zn, and O in $Sr_2Nd_2Zn_2O_7$. (e) Calculated negative-signed COHPs for Nd–O, Sr–O, and Zn–O bonds.

Open Access Article. Published on 18 December 2024. Downloaded on 2/10/2026 7:04:31 AM. This article is licensed under a Creative Commons Attribution-NonCommercial 3.0 Unported Licence.

constant, and ν is the frequency), the band gap is estimated to be $E_g = 3.81$ eV.

DFT calculations were carried out to gain insight into the optical properties and the bonding characteristics of $Sr_2Nd_2Zn_2O_7$. The calculated electronic band structure in Fig. 7b and c reveals that the conduction band minimum (CBM) and the valence band maximum (VBM) are both located at the Γ points of the Brillouin zone, indicative of a direct semiconductor with a band gap value of $E_g \approx 2.15$ eV for $Nd_2Sr_2Zn_2O_7$. This calculated E_g value is much smaller than the experimental value deduced from the UV-vis diffusion spectra due to the inaccurate approximation of the exchange–correlation energy of the DFT calculations. The density of states (DOS) in Fig. 7d shows that the CBM is composed of O 2p and Zn 4s states, and the VBM mainly comprises the nonbonding O 2p states, implying that the optical property of $Nd_2Sr_2Zn_2O_7$ is only dictated by the $[Zn_2O_7]^{5-}$ ladder. Moreover, the COHP plots of metal–oxygen pairs in Fig. 7e demonstrate the strong covalent bonding feature of the Zn–O pair and the VBM of $Nd_2Sr_2Zn_2O_7$ is in fact composed of the occupied Zn 3d–O 2p anti-bonding states. The Nd–O pair also show larger bonding and antibonding values, evidencing the covalent bonding character between Nd^{3+} and O^{2-}. In contrast, the interaction between Sr^{2+} and O^{2-} ions is an ionic bond due to the negligible −COHP values for the Sr–O pair. The integrated COHP (ICOHP) values in the sequence of Zn–O (−2.99 eV) < Nd–O (−2.32 eV) < Sr–O (−0.29 eV) indicate a gradual weakening trend of covalent bonding, which is fairly consistent with the electronegativities for the metals of Zn (1.65) > Nd (1.14) > Sr (0.95).

3.6 Transport properties

3.6.1 Mixed electronic and oxide ionic conductivity. The transport properties of $Sr_2Nd_2Zn_2O_7$ ceramic materials were comprehensively investigated by electrochemical impedance spectroscopy over the temperature range of 300–1000 °C under

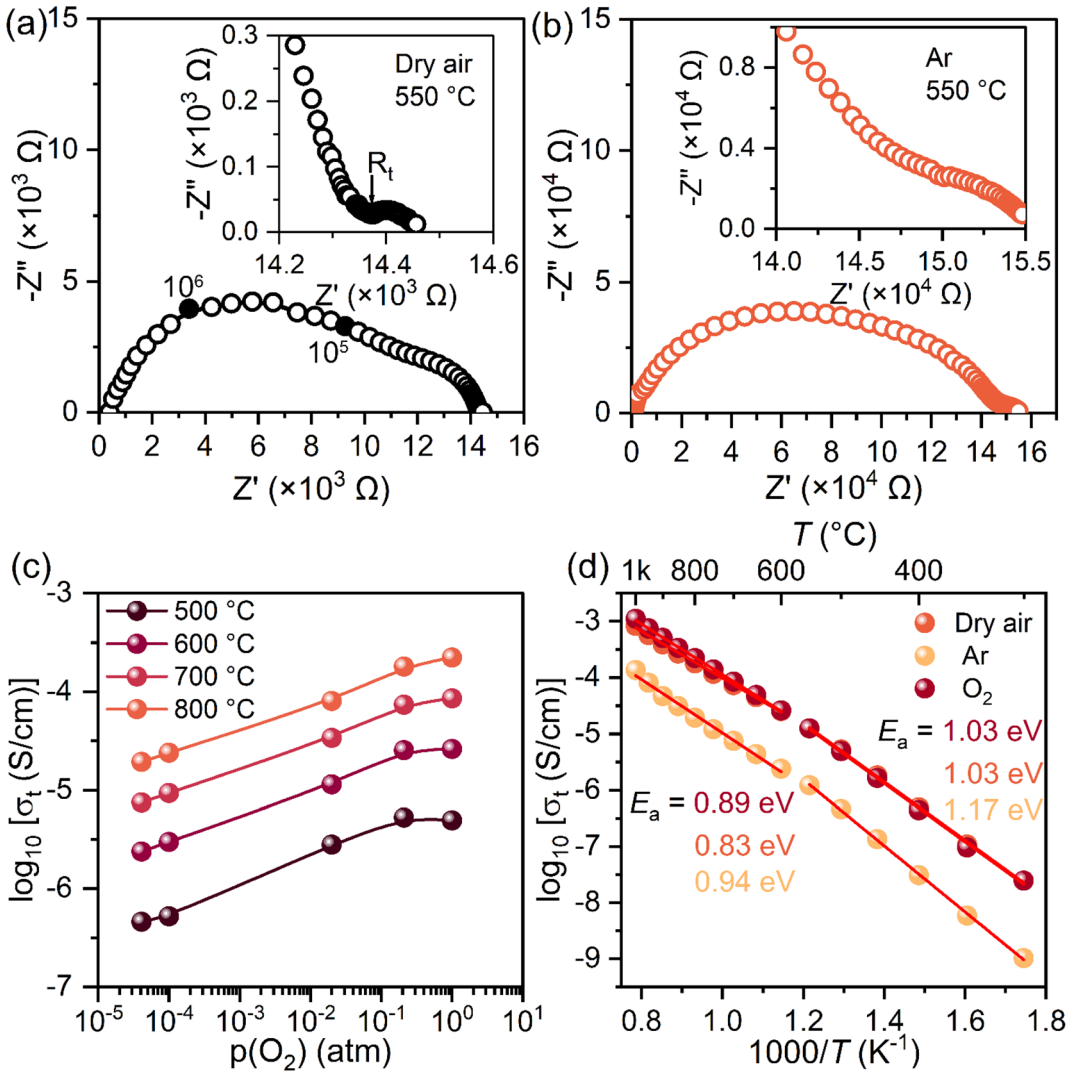

Fig. 8 Complex impedance spectra for $Sr_2Nd_2Zn_2O_7$ recorded at 550 °C under dry air (a) and Ar (b) atmospheres. Insets of (a) and (b) show enlargements of the impedance spectra in the low-frequency region. (c) $p(O_2)$ dependence of conductivities of $Sr_2Nd_2Zn_2O_7$ at different temperatures. (d) Arrhenius plots of total conductivities of $Sr_2Nd_2Zn_2O_7$ under various atmospheres.

© 2025 The Author(s). Published by the Royal Society of Chemistry

Open Access Article. Published on 18 December 2024. Downloaded on 2/10/2026 7:04:31 AM. This article is licensed under a Creative Commons Attribution-NonCommercial 3.0 Unported Licence.

various atmospheres. Fig. 8a shows the Nyquist plot of complex impedance spectra recorded at 550 °C under dry air conditions, which exhibits two well-resolved semicircles in the high and intermediate frequency ranges. A spectroscopic plot of capacity (C) *versus* frequency shows two frequency-independent plateaus with capacities of $\sim 2.0 \times 10^{-11}$ and 2.1×10^{-10} F cm^{-1} in the high and intermediate frequencies, respectively (see Fig. S6†). This result implies that the large and small arcs in the high- and intermediate-frequency ranges are attributed to the bulk and grain contributions, respectively, and the total conductivity of $Sr_2Nd_2Zn_2O_7$ is dominated by the bulk contribution. A close inspection of the low-frequency range (0.1–10 Hz) reveals a very small semicircle with capacities within 1.0–9.3 $\times 10^{-8}$ F cm^{-1} (see Fig. 8a and S6†), which can be attributed to the electrode response and indicative of oxide ionic conduction. The semicircle in the low-frequency range becomes much more flatter instead of a pronounced Warburg-type inclined line under Ar conditions, signifying that the ionic contribution in $Sr_2Nd_2Zn_2O_7$ is very limited (see Fig. 8b). Impressively, the total resistance measured in Ar conditions is one order of magnitude higher than those obtained in dry air and O_2 conditions at the same temperature (see Fig. 8a, b and S7†). Further impedance spectra were collected with oxygen partial pressure $p(O_2)$ ranging from 10^{-5} to 1 atm, showing that the total conductivity is in proportion to $p(O_2)$ and thus signifying a p-type conduction behavior for $Sr_2Nd_2Zn_2O_7$. The above results altogether demonstrate that $Sr_2Nd_2Zn_2O_7$ is a mixed electronic and oxide-ionic conductor and the contribution of oxide ion conduction to the total conduction should be very limited. The origin of p-type electronic conduction in $Sr_2Nd_2Zn_2O_7$ could be rationalized by the absorption of oxygen from high-concentration O_2 atmospheres by the intrinsic oxygen vacancies in the lattice according to the following electrochemical reaction equation:

$$\frac{1}{2}O_2 + V_O^{\cdot\cdot} \leftrightarrow O_O^{\times} + 2h^{\cdot}$$

where $V_O^{\cdot\cdot}$ and $O_O^{\times}$ indicate unoccupied and occupied oxygen sites in the lattice, respectively, and $h^{\cdot}$ represents a hole according to the Kroger–Vink notation.[63]

Arrhenius plots of total conductivity, σ_t, *versus* reciprocal temperature in Fig. 8d show that σ_t measured in Ar condition is an order of magnitude lower than those obtained in dry air and O_2 conditions over the entire temperature range, consolidating the mixed conduction behavior under dry air and O_2 atmospheres. At 700 °C, σ_t reaches $\sim 10^{-4}$ S cm^{-1} in dry air, which is comparable to other mixed electronic and oxide ionic conductors at the same temperature, such as $La_{0.7}Sr_{2.3}GaO_{4.85}$ ($\sim 10^{-4}$ S cm^{-1}),[64] $BaNdInO_4$ ($\sim 7.5 \times 10^{-5}$ S cm^{-1}),[65] $K_{0.5}Bi_{0.5+x}TiO_{3+3x/2}$ ($\sim 10^{-4}$ S cm^{-1}).[66] The σ_t increases along with temperature and conspicuous changes in slope are observed at temperatures higher than 600 °C, associated with a significant lowering in the apparent activation energies (E_a) from 1.03–1.17 to 0.83–0.94 eV. Such activation energy lowering at high temperatures is usually attributed to temperature-driven structural rearrangement, phase transition, and change in predominate charge carriers.

Table 3 Oxygen transport number $t_{O^{2-}}$ values for $Sr_2Nd_2Zn_2O_7$

T (°C)	$EMF_{cal.}$ (mV)	$EMF_{exp.}$ (mV)	$t_{O^{2-}}$
500	65.14	12.5	0.19
600	73.57	25.2	0.34
700	82.00	30.1	0.37
800	90.42	34.8	0.38

To decipher the plausible predominant charge carrier change in $Sr_2Nd_2Zn_2O_7$ at elevated temperatures, we carried out EMF measurements on an oxygen concentration cell at temperatures from 500 to 800 °C. The calculated and experimental EMF values and the corresponding oxygen transport numbers ($t_{O^{2-}}$) are listed in Table 3. At 500 °C, the measured EMF value of 12.5 mV is significantly smaller than the calculated value (65.14 mV), resulting in a $t_{O^{2-}}$ value as small as 0.19 and thus firmly consolidating the mixed oxide ion and electron conduction behavior for $Sr_2Nd_2Zn_2O_7$. At temperatures higher than 600 °C, $t_{O^{2-}}$ is enhanced significantly to > 0.3 and increases slightly along with temperature. Hence, the improvement in $t_{O^{2-}}$ suggests that the slope change in Arrhenius plots at elevated temperatures should be attributed to the dramatic enhancement in oxide ionic contribution to the total conductivity. The enhancement in oxide ionic conduction at high temperatures is plausibly attributed to the ordering-to-disordering phase transition, warranted to be confirmed by *in situ* PXRD. The high mixed electronic and oxide ion total conductivity (> 10^{-4} S cm^{-1}) together with the relatively high oxygen transport number indicates the potential application in gas separation.

3.6.2 Oxide ionic migration mechanism. To decipher the oxide ion transport mechanism in the $Sr_2Nd_2Zn_2O_7$ orthorhombic matrix, the bond valence site energy (BVSE) method implemented in the SoftBV software was used to find the local minima and saddle points by analyzing the energy level of each point in the energy landscape and connect them by tracking from saddle-point voxels to minima voxels to construct the transport network.[67,68] This method has been widely used for high-throughput analysis of ion transport pathways for Li^+, Na^+, and O^{2-} conductors, showing efficient, informative, and credible ion migration pathways. The BVSE landscape with an isosurface energy of −1.5 eV for $Sr_2Nd_2Zn_2O_7$ is delineated in Fig. 9a. One-dimensional (1D) oxide ion migration pathways along the [010] direction that links the discrete $[Zn_2O_7]^{10-}$ ladders could be vividly visualized in Fig. 9a. This conduction pathway involves the O1 and O3 ions and interstitial $i1$ and $i2$ sites in proximate to the oxygen-vacant sites, implying that the trigger of the long-range ionic conduction is the jump of the O1 and O3 ions into the interstitial sites (oxygen-vacancy exchange). This 1D O1/O3 ↔ $i1$/$i2$ ↔ O1/O3 pathway needs to overcome a bond valence energy barrier as high as 0.97 eV to pass through a saddle point ($S2$) located at (0, 0.667, 0.052) (see Fig. 9c). It is widely accepted that the terminal oxygen ions provide additional freedom to exchange oxygen positions in a flexible framework and thus play a decisive role in ionic conduction. However, the energy barriers for the terminal O4 and O5 jumping to the interstitial $i1$ site are 1.43 and 1.47 eV,

Open Access Article. Published on 18 December 2024. Downloaded on 2/10/2026 7:04:31 AM.
This article is licensed under a Creative Commons Attribution-NonCommercial 3.0 Unported Licence.

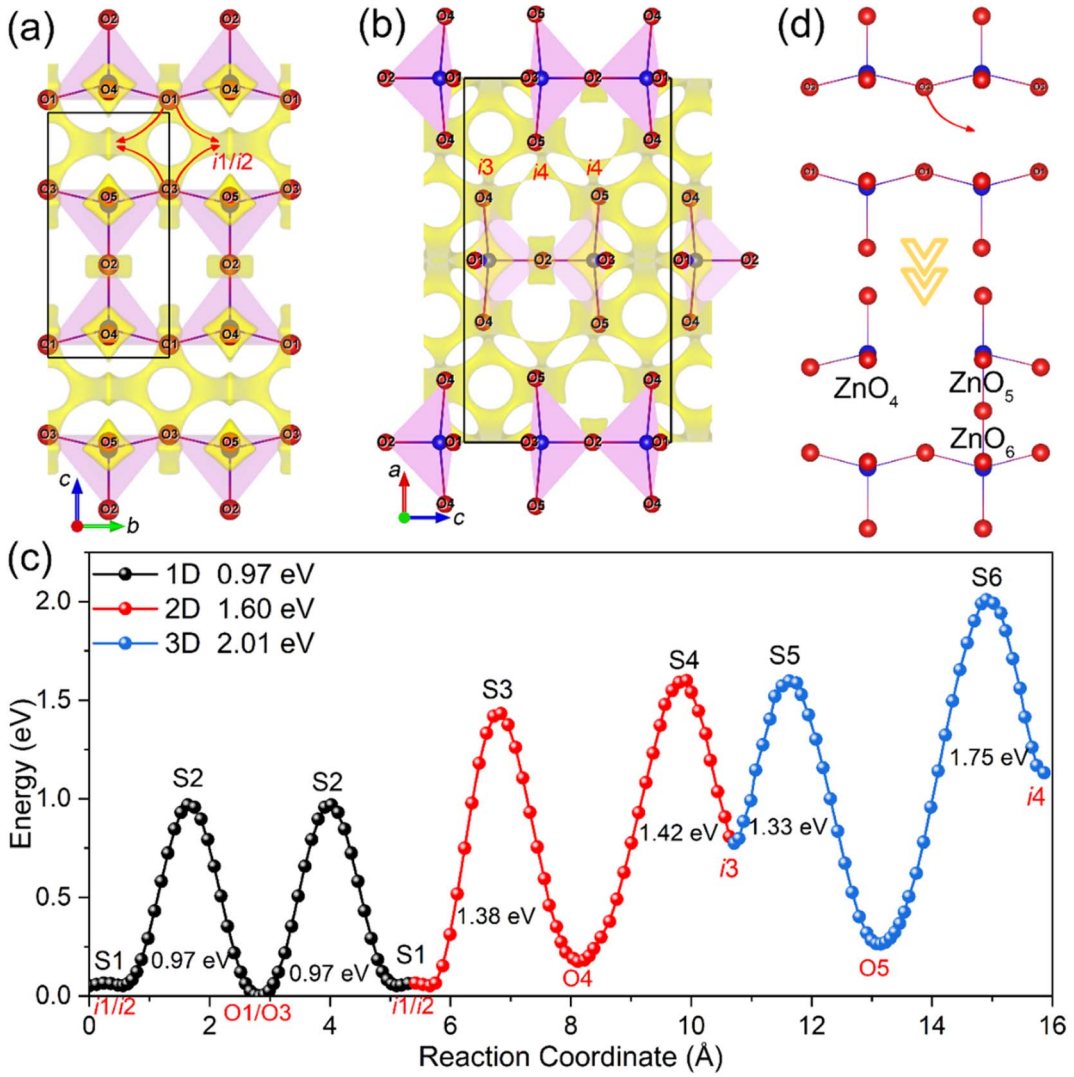

Fig. 9 BVSE landscapes for oxide ions in $Sr_2Nd_2Zn_2O_7$ with isosurface energy of −1.5 (a) and −0.7 eV (b). (c) Migration energy barriers for oxide ions in different dimensional pathways. (d) Scheme of the local coordination geometry for Zn^{2+} cations before and after the migration of the bridging O1/O3 ions. The A-site cations in (a and b) are omitted for clarity.

respectively, which are significantly higher than those of O1/O3 ↔ *i*1/*i*2, plausibly due to the significantly longer Zn–O4/O5 bond lengths induced longer O4/O5−*i*1 distances and thus higher energy barriers. Moreover, the motion of the bridging O2 ion is rather localized, suppressed by bonding to two Zn cations with bond lengths as short as 1.86 Å. A three-dimensional (3D) conduction pathway involving O1, O3, O4, O5 and two additional interstitial sites (*i*3 and *i*4) in the rock-salt layers can be envisaged in Fig. 9b. Note that the partial occupation of the interstitial sites in the rock-salt layer of the hyperstoichiometric $Ln_2NiO_{4+\delta}$ is the structural origin of fast oxide ion conduction. Here, the energy barrier of > 1.6 eV for the 3D O4/O5 ↔ *i*3/*i*4 ↔ O4/O5 pathways is significantly higher than that of the 1D pathway along the *b*-axis (see Fig. 9c), arising from unoccupied interstitial sites. The above results altogether indicate that the oxide ionic conduction of $Sr_2Nd_2Zn_2O_7$ should be one-dimensional.

This gate-control oxide migration pathway is reminiscent of the oxide ionic conduction mechanism of brownmillerite $A_2B_2O_5$, which is derived from ABO_3 perovskite by removing parallel ⟨110⟩ arrays of oxygen ions to create alternating layers of BO_4 and BO_6 metal–oxygen polyhedra arranged in corner-linked chains and sheets, respectively. The trigger of oxide ionic conduction in $A_2B_2O_5$ is the jump of the apical oxygen (the bridge oxygen that links BO_4 and BO_6) of the BO_6-octahedron to the interstitial position (oxygen-vacant site) in the tetrahedral layer, leaving oxygen vacancies in the octahedral layer and thus realizing ionic conduction *via* oxygen-vacancy exchange.[69–71] This gate-like ionic conduction mechanism in $A_2B_2O_5$ leads to the deformation of interconnected BO_6 and BO_4 into discrete BO_5 square pyramids and BO_4 tetrahedra in the local scale structure. Here in $Sr_2Nd_2Zn_2O_7$, the escape of the basal-plane oxygens (O1 and O3) into the interstitial sites leads to the formation of significantly distorted ZnO_4 and reorientated ZnO_5

© 2025 The Author(s). Published by the Royal Society of Chemistry

Open Access Article. Published on 18 December 2024. Downloaded on 2/10/2026 7:04:31 AM.
This article is licensed under a Creative Commons Attribution-NonCommercial 3.0 Unported Licence.

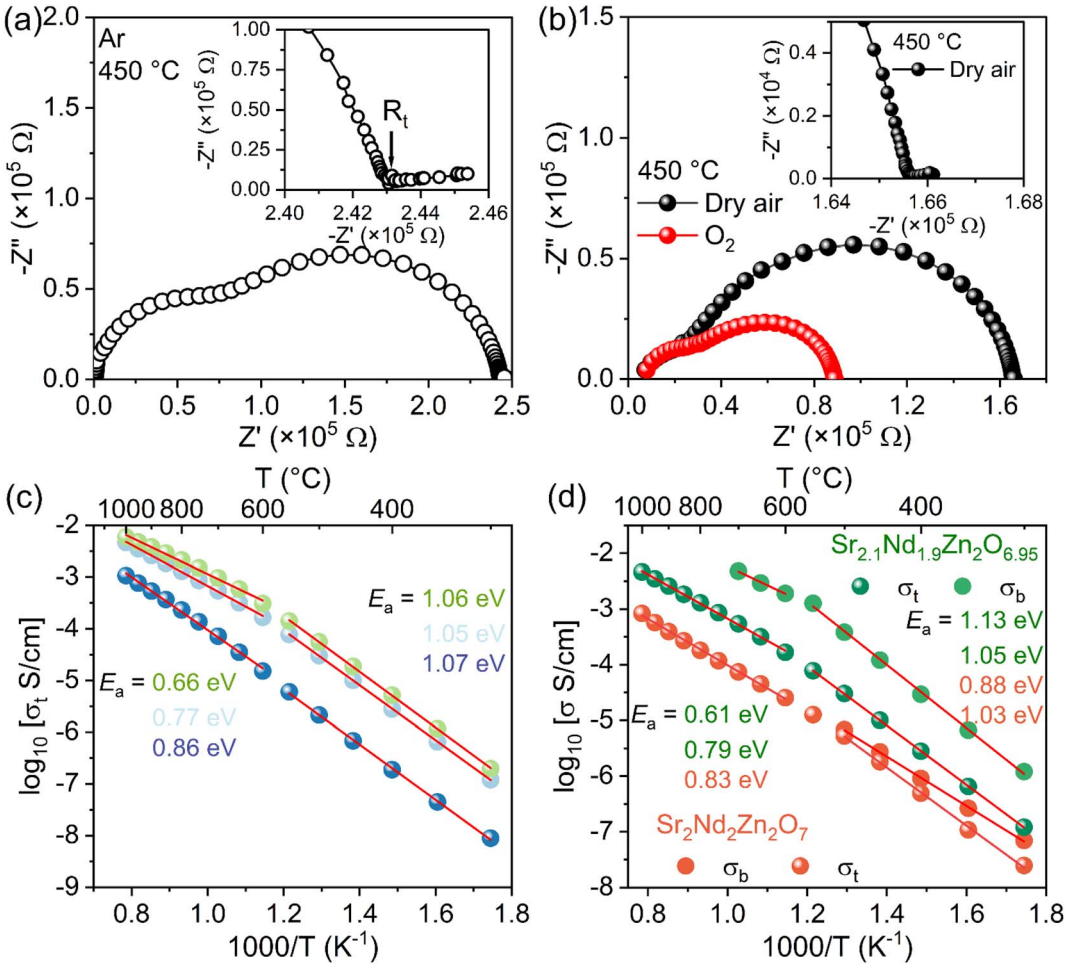

Fig. 10 Complex impedance spectra for $Sr_{2.1}Nd_{1.9}Zn_2O_{6.95}$ recorded at 450 °C under Ar (a) and day air and O_2 (b) atmospheres. Insets of (a) and (b) show enlargements of the impedance spectra in the low frequency region. (c) Arrhenius plots of total conductivities of $Sr_{2.1}Nd_{1.9}Zn_2O_{6.95}$ under various atmospheres. (d) Conductivity comparison between pristine $Sr_2Nd_2Zn_2O_7$ and accepter doped $Sr_{2.1}Nd_{1.9}Zn_2O_{6.95}$.

square pyramids that point along the *b*-axis and links to newly reformed ZnO_6 octahedra (see Fig. 9d).

According to the above proposed gate-like conduction mechanism, the ionic conduction component of $Sr_2Nd_2Zn_2O_7$ should be further enhanced by introducing excess oxygen vacancies. To further verify this mechanism, we deliberately prepared an acceptor-doped composition $Sr_{2.1}Nd_{1.9}Zn_2O_{6.95}$. The Rietveld refinement plot of PXRD data in Fig. S8† confirms that $Sr_{2.1}Nd_{1.9}Zn_2O_{6.95}$ is phase pure. The complex impedance spectra recorded at 450 °C under different atmospheres are shown in Fig. 10a and b. Pronounced inclined lines in the low-frequency range, indicative of oxide ionic conduction, could be observed for the acceptor doped $Sr_{2.1}Nd_{1.9}Zn_2O_{6.95}$, in sharp contrast to those of the pristine $Sr_2Nd_2Zn_2O_7$. $Sr_{2.1}Nd_{1.9}Zn_2O_{6.95}$ is still a mixed ionic and electronic conductor as hinted by the significantly lower total conductivity under the Ar atmosphere compared to those in dry air and O_2 conditions (Fig. 10a–c). A comparison of conductivities between pristine $Sr_2Nd_2Zn_2O_7$ and acceptor-doped $Sr_{2.1}Nd_{1.9}Zn_2O_{6.95}$ is shown in Fig. 10d, where the bulk conductivity, σ_b, conductivities of $Sr_{2.1}Nd_{1.9}Zn_2O_{6.95}$ are two orders of magnitude higher than those of $Sr_2Nd_2Zn_2O_7$. At temperatures higher than 800 °C, the total conductivity of $Sr_{2.1}Nd_{1.9}Zn_2O_{6.95}$ in air is higher than 1.0×10^{-3} S cm^{-1}, highlighting its great application potential in energy generation and storage devices. Note that compared to E_a = 0.88 eV of σ_b for $Sr_2Nd_2Zn_2O_7$ in the low-temperature range, the significantly higher E_a of 1.13 eV for $Sr_{2.1}Nd_{1.9}Zn_2O_{6.95}$ should be undoubtedly attributed to a dramatic enhancement of the ionic contribution to σ_b. The ionic conductivity enhancement realized by acceptor doping for $Sr_{2.1}Nd_{1.9}Zn_2O_{6.95}$, in turn, underpins the gate-like ionic conduction mechanism for oxygen-vacancy ordered $Sr_2Nd_2Zn_2O_7$. Moreover, the conductivity of $Sr_{2.1}Nd_{1.9}Zn_2O_{6.95}$ at around 300 °C ($\sim 1.2 \times 10^{-6}$ S cm^{-1}) is comparable to the H^- conductivities of those H^-/O^{2-} ordered $n = 1$ RP perovskite-type oxyhydride materials at the same temperature, such as Ln_2LiO_3H ($< 5 \times 10^{-6}$ S cm^{-1}),[59] Ba_2ScO_3H (5.2×10^{-6} S cm^{-1}),[72] and Ba_2YO_3H ($\sim 1.0 \times 10^{-5}$ S cm^{-1}),[73] but significantly lower than that of $Ba_{1.75}LiO_{0.9}H_{2.7}$ ($\sim 1.0 \times 10^{-2}$ S cm^{-1}), which has a high H^--content and exhibits H^-/O^{2-} disordering.[58] Additionally, the activation energy for oxide ionic conduction is also higher than that for hydride ion conduction, which can be attributed to the greater charge, larger size, and mass of O^{2-} compared to H^-.

© 2025 The Author(s). Published by the Royal Society of Chemistry

Open Access Article. Published on 18 December 2024. Downloaded on 2/10/2026 7:04:31 AM. This article is licensed under a Creative Commons Attribution-NonCommercial 3.0 Unported Licence.

4. Conclusion

We report the rational design and crystal structure of a new oxygen-deficient $n = 1$ RP perovskite $Nd_2Sr_2Zn_2O_7$. Regarding the aristotype *I*4/*mmm*-RP structure, $Nd_2Sr_2Zn_2O_7$ possesses a 2-fold *Pmmn*-superstructure stemming from oxygen-vacancy-column ordering in the perovskite layer, as confirmed by the combined Rietveld refinements of high-resolution monochromatic X-ray diffraction and neutron powder diffraction data. A comprehensive analysis of structures deciphered that the oxygen vacancy ordering in $Nd_2Sr_2Zn_2O_7$ is maintained by the A-site column-ordered Nd/Sr cations with a large difference in ionic radii. As a result, the oxygen vacancy ordering and A-site cation ordering in $Nd_2Sr_2Zn_2O_7$ are coupled. Moreover, we found that the oxygen vacancies in the $n = 1$ RP perovskite are in fact confined to the equatorial sites of the BO_6-octahedra, which can reduce the cationic A–A/B repulsion to the greatest extent and is in stark contrast to the structurally favorable inner apical oxygen vacancies in $n \geq 2$ structures. $Nd_2Sr_2Zn_2O_7$ is a direct-gap semiconductor with a band gap of ~3.8 eV and exhibits mixed ion-electron conductivity with a limited ionic contribution to the total conductivity due to oxygen-vacancy ordering. The oxide ionic conduction in $Nd_2Sr_2Zn_2O_7$ is mediated by the migration of the bridging oxygen ions to the oxygen-vacant sites, affording a gate-like ionic motion along the $[Zn_2O_7]$-ladders. Our work offers new insights into the crystal chemistry of oxygen-deficient $n = 1$ RP perovskites, which gives a path toward new functional RP-structure design.

Data availability

The data supporting this article have been included as part of the ESI.†

Author contributions

Pengfei Jiang and Tao Yang designed and guided the project. Maxim Avdeev collected the NPD data, provided important advice on data analysis, and reviewed the manuscript. Danhe Li and Guangxiang Lu performed the majority of the experiments. Zien Cheng and Zhengyang Zhou collected and analyzed the 3D ED data. Jungu Xu helped with EMF measurements. Rihong Cong reviewed the manuscript and provided advice on manuscript revision. Pengfei Jiang wrote the manuscript with contributions from all the authors.

Conflicts of interest

The authors declare no competing financial interest.

Acknowledgements

This work is financially supported by the National Natural Science Foundation of China (no. 22271030, 22171031, and 22171032), Natural Science Foundation of Chongqing (no. cstc2021jcyj-msxmX0971), and Fundamental Research Funds for the Central Universities (no. 2024CDJXY010).

References

1 H. L. Sun, M. W. Huo, X. W. Hu, J. Y. Li, Z. J. Liu, Y. F. Han, L. Y. Tang, Z. Q. Mao, P. T. Yang, B. S. Wang, J. G. Cheng, D.-X. Yao, G.-M. Zhang and M. Wang, Signatures of superconductivity near 80 K in a nickelate under high pressure, *Nature*, 2023, **621**, 493–498.

2 H. Sakakibara, N. Kitamine, M. Ochi and K. Kuroki, Possible High T_c Superconductivity in $La_3Ni_2O_7$ under High Pressure through Manifestation of a Nearly Half-Filled Bilayer Hubbard Model, *Phys. Rev. Lett.*, 2024, **132**, 106002.

3 M. J. Pitcher, P. Mandal, M. S. Dyer, J. Alaria, P. Borisov, H. J. Niu, J. B. Claridge and M. J. Rosseinsky, Tilt engineering of spontaneous polarization and magnetization above 300 K in a bulk layered perovskite, *Science*, 2015, **347**, 420–424.

4 Y. S. Oh, X. Luo, F.-T. Huang, Y. Z. Wang and S.-W. Cheong, Experimental demonstration of hybrid improper ferroelectricity and the presence of abundant charged walls in $(Ca,Sr)_3Ti_2O_7$ crystals, *Nat. Mater.*, 2015, **14**, 407–413.

5 S. Yoshida, H. Akamatsu, R. Tsuji, O. Hernandez, H. Padmanabhan, A. Sen Gupta, A. S. Gibbs, K. Mibu, S. Murai, J. M. Rondinelli, V. Gopalan, K. Tanaka and K. Fujita, Hybrid improper ferroelectricity in $(Sr,Ca)_3Sn_2O_7$ and beyond: universal relationship between ferroelectric transition temperature and tolerance factor in n = 2 Ruddlesden–Popper Phases, *J. Am. Chem. Soc.*, 2018, **140**, 15690–15700.

6 W. Yi, T. Kawasaki, Y. Zhang, H. Akamatsu, R. Ota, S. Torii and K. Fujita, $La_2SrSc_2O_7$: A-Site Cation Disorder Induces Ferroelectricity in Ruddlesden–Popper Layered Perovskite Oxide, *J. Am. Chem. Soc.*, 2024, **146**, 4570–4581.

7 D. M. Halat, R. Dervişoğlu, G. Kim, M. T. Dunstan, F. Blanc, D. S. Middlemiss and C. P. Grey, Probing Oxide-Ion Mobility in the Mixed Ionic–Electronic Conductor $La_2NiO_{4+\delta}$ by Solid-State ^{17}O MAS NMR Spectroscopy, *J. Am. Chem. Soc.*, 2016, **138**, 11958–11969.

8 A. Maity, R. Dutta, O. Sendtskyi, M. Ceretti, A. Lebranchu, D. Chernyshov, A. Bosak and W. Paulus, Exploring Fast Room Temperature Oxygen Diffusion in $Pr_2NiO_{4+\delta}$ Stand-Alone Single-Crystalline Electrodes, *Chem. Mater.*, 2022, **34**, 414–421.

9 M. S. Senn, A. Bombardi, C. A. Murray, C. Vecchini, A. Scherillo, X. Luo and S.-W. Cheong, Negative Thermal Expansion in Hybrid Improper Ferroelectric Ruddlesden-Popper Perovskites by Symmetry Trapping, *Phys. Rev. Lett.*, 2015, **114**, 035701.

10 Y. J. Zhang, J. Wang and P. Ghosez, Unraveling the Suppression of Oxygen Octahedra Rotations in $A_3B_2O_7$ Ruddlesden-Popper Compounds: Engineering Multiferroicity and Beyond, *Phys. Rev. Lett.*, 2020, **125**, 157601.

11 M. S. Senn, C. A. Murray, X. Luo, L. Wang, F.-T. Huang, S.-W. Cheong, A. Bombardi, C. Ablitt, A. A. Mostofi and N. C. Bristowe, Symmetry Switching of Negative Thermal

© 2025 The Author(s). Published by the Royal Society of Chemistry

Open Access Article. Published on 18 December 2024. Downloaded on 2/10/2026 7:04:31 AM. This article is licensed under a Creative Commons Attribution-NonCommercial 3.0 Unported Licence.

Expansion by Chemical Control, *J. Am. Chem. Soc.*, 2016, **138**, 5479.

12 Q. Wang, M. Nakabayashi, T. Hisatomi, S. Sun, S. Akiyama, Z. Wang, Z. H. Pan, X. Xiao, T. Watanabe, T. Yamada, N. Shibata, T. Takata and K. Domen, Oxysulfide photocatalyst for visible-light-driven overall water splitting, *Nat. Mater.*, 2019, **18**, 827–832.

13 K. Wang, C. Han, Z. P. Shao, J. H. Qiu, S. B. Wang and S. M. Liu, Perovskite Oxide Catalysts for Advanced Oxidation Reactions, *Adv. Funct. Mater.*, 2021, **31**, 2102089.

14 R. H. Zhang, M. S. Senn and M. A. Hayward, Directed Lifting of Inversion Symmetry in Ruddlesden–Popper Oxide–Fluorides: Toward Ferroelectric and Multiferroic Behavior, *Chem. Mater.*, 2016, **28**, 8399–8406.

15 P. V. Balachandran, D. Puggioni and J. M. Rondinelli, Crystal-Chemistry Guidelines for Noncentrosymmetric A_2BO_4 Ruddlesden–Popper Oxides, *Inorg. Chem.*, 2014, **53**, 336–348.

16 H. Akamatsu, K. Fujita, T. Kuge, A. S. Gupta, A. Togo, S. Lei, F. Xue, G. Stone, J. M. Rondinelli, L.-Q. Chen, I. Tanaka, V. Gopalan and K. Tanaka, Inversion Symmetry Breaking by Oxygen Octahedral Rotations in the Ruddlesden-Popper $NaRTiO_4$ Family, *Phys. Rev. Lett.*, 2014, **112**, 187602.

17 S. Yoshida, H. Akamatsu, A. S. Gibbs, S. Kawaguchi, V. Gopalan, K. Tanaka and K. Fujita, Interplay between Oxygen Octahedral Rotation and Deformation in the Acentric $ARTiO_4$ Series toward Negative Thermal Expansion, *Chem. Mater.*, 2022, **34**, 6492–6504.

18 Z. H. Dong, M. W. Huo and J. Li, Visualization of oxygen vacancies and self-doped ligand holes in $La_3Ni_2O_{7-\delta}$, *Nature*, 2024, **630**, 847–852.

19 Y. B. Liu, J. W. Mei, F. Ye, W. Q. Chen and F. Yang, $s_{\pm}$-wave pairing and the destructive role of apical-oxygen deficiencies in $La_3Ni_2O_7$ under pressure, *Phys. Rev. Lett.*, 2023, **131**, 236002.

20 Y. Zhang, L.-F. Lin, A. Moreo, T. A. Maier and E. Dagotto, Electronic structure, magnetic correlations, and superconducting pairing in the reduced Ruddlesden–Popper bilayer $La_3Ni_2O_6$ under pressure: different role of d_{3z2-r2} orbital compared with $La_3Ni_2O_7$, *Phys. Rev. B*, 2024, **109**, 045151.

21 R. Dutta, A. Maity, A. Marsicano, M. Ceretti, D. Chernyshov, A. Bosak, A. Villesuzanne, G. Roth, G. Perversi and W. Paulus, Long-range oxygen ordering linked to topotactic oxygen release in $Pr_2NiO_{4+\delta}$ fuel cell cathode material, *J. Mater. Chem. A*, 2020, **8**, 13987–13995.

22 M. Yashima, M. Enoki, T. Wakita, R. Ali, Y. Matsushita, F. Izumi and T. Ishihara, Structural Disorder and Diffusional Pathway of Oxide Ions in a Doped Pr_2NiO_4-Based Mixed Conductor, *J. Am. Chem. Soc.*, 2008, **130**, 2762–2763.

23 M. Yashima, H. Yamada, S. Nuansaeng and T. Ishihara, Role of Ga^{3+} and Cu^{2+} in the High Interstitial Oxide-Ion Diffusivity of Pr_2NiO_4-Based Oxides: Design Concept of Interstitial Ion Conductors through the Higher-Valence d^{10} Dopant and Jahn-Teller Effect, *Chem. Mater.*, 2012, **24**, 4100–4113.

24 M. Avdeev and J. R. Hester, ECHIDNA: A Decade of High-Resolution Powder Diffraction at OPAL, *J. Appl. Crystallogr.*, 2018, **51**, 1597–1604.

25 A. A. Coelho, An indexing algorithm independent of peak position extraction for X-ray powder diffraction patterns, *J. Appl. Crystallogr.*, 2017, **50**, 1323–1330.

26 A. A. Coelho, TOPAS and TOPAS-Academic: an optimization program integrating computer algebra and crystallographic objects written in C++, *J. Appl. Crystallogr.*, 2018, **51**, 210–218.

27 L. Palatinus, P. Brázda, M. Jelínek, J. Hrdá, G. Steciuk and M. Klementová, Specifics of the data processing of precession electron diffraction tomography data and their implementation in the program PETS2.0, *Acta Crystallogr., Sect. B*, 2019, **75**, 512–522.

28 J. Hafner, *Ab initio* simulations of materials using VASP: Density-functional theory and beyond, *J. Comput. Chem.*, 2008, **29**, 2044–2078.

29 P. E. Blöchl, Projector augmented-wave method, *Phys. Rev. B*, 1994, **50**, 17953–17979.

30 J. P. Perdew, K. Burke and M. Ernzerhof, Generalized gradient approximation made simple, *Phys. Rev. Lett.*, 1996, **77**, 3865–3868.

31 H. T. Stokes, D. M. Hatch and B. J. Campbell, *ISODISTORT, ISOTROPY Software Suite*, **https://www.iso.byu.edu**.

32 B. J. Campbell, H. T. Stokes, D. E. Tanner and D. M. Hatch, ISODISPLACE: An Internet Tool for Exploring Structural Distortions, *J. Appl. Crystallogr.*, 2006, **39**, 607–614.

33 R. D. Shannon, Revised Effective Ionic Radii and Systematic Studies of Interatomic Distances in Haildes and Chalcogenides, *Acta Crystallogr., Sect. A*, 1976, **32**, 751–767.

34 I. D. Brown and D. Altermatt, Bond-Valence Parameters Obtained from a Systematic Analysis of the Inorganic Crystal Structure Database, *Acta Crystallogr., Sect. B: Struct. Sci.*, 1985, **41**, 244–247.

35 S. W. Li and Y. F. Ren, The synthesis and physical properties of the new layered lanthanide alkaline earth cobalt oxides $[Ln_2MCo_2O_7$ (Ln=Sm, Gd; M=Sr, Ba)], *Mater. Res. Bull.*, 1994, **29**, 993–1000.

36 J. Meng, H. Satoh, M. Ishida and N. Kamegashira, Phase transition of $BaNd_2Mn_2O_7$, *J. Alloys Compd.*, 2006, **408**, 1182–1186.

37 N. N. M. Gurusinghe, J. de la Figuera, J. F. Marco, M. F. Thomas, F. J. Berry and C. Greaves, Synthesis and characterisation of the $n = 2$ Ruddlesden-Popper phases $Ln_2Sr(Ba)Fe_2O_7$ (Ln = La, Nd, Eu), *Mater. Res. Bull.*, 2013, **48**, 3537–3544.

38 J. A. Rodgers, P. D. Battle, N. Dupré, C. P. Grey and J. Sloan, Cation and spin ordering in the $n = 1$ Ruddlesden-Popper phase $La_2Sr_2LiRuO_8$, *Chem. Mater.*, 2004, **16**, 4257–4266.

39 M. T. Weller and D. R. Lines, Structure and oxidation-state relationships in ternary copper oxides, *J. Solid State Chem.*, 1989, **82**, 21–29.

40 C. Tassel, L. Seinberg, N. Hayashi, S. Ganesanpotti, Y. Ajiro, Y. Kobayashi and H. Kageyama, Sr_2FeO_3 with Stacked Infinite Chains of FeO_4 Square Planes, *Inorg. Chem.*, 2013, **52**, 6096–6102.

Open Access Article. Published on 18 December 2024. Downloaded on 2/10/2026 7:04:31 AM. This article is licensed under a Creative Commons Attribution-NonCommercial 3.0 Unported Licence.

41 R. G. Palgrave and M. A. Hayward, Structure and Magnetism of (La/Sr)$M_{0.5}Ir^{V}_{0.5}O_4$ and Topochemically Reduced (La/Sr)$M_{0.5}Ir^{II}_{0.5}O_3$ (M = Fe, Co) Complex Oxides, *Inorg. Chem.*, 2019, **58**, 6336–6343.

42 J. Hadermann, O. Pérez, N. Créon, C. Michel and M. Hervieu, The (3 + 2)D structure of oxygen deficient $LaSrCuO_{3.52}$, *J. Mater. Chem.*, 2007, **17**, 2344–2350.

43 M. E. Leonowicz, K. R. Poeppelmeier and J. M. Longo, Structure determination of Ca_2MnO_4 and $Ca_2MnO_{3.5}$ by X-ray and neutron methods, *J. Solid State Chem.*, 1985, **59**, 71–80.

44 L. J. Gillie, A. J. Wright and J. Hadermann, Synthesis and characterization of the reduced single-layer manganite $Sr_2MnO_{3.5+x}$, *J. Solid State Chem.*, 2002, **167**, 145–151.

45 M. Caldes, C. Michel, T. Rouillon, M. Hervieu and B. Raveau, Novel indates $Ln_2BaIn_2O_7$, $n = 2$ members of the Ruddlesden-Popper family (Ln = La, Nd), *J. Mater. Chem.*, 2002, **12**, 473–476.

46 G. M. Sarjeant, K. B. Greenwood, K. R. Poeppelmeier, H. Zhang, P. A. Salvador, T. O. Mason and L. D. Marks, Synthesis and structure of $LaSr_2CuTiO_{6.5}$: A new oxygen-deficient Ruddlesden-Popper phase, *Chem. Mater.*, 1996, **8**, 2792–2798.

47 J. A. Sannes, R. K. Kizhake Malayil, L. T. Corredor, A. U. B. Wolter, H.-J. Grafe and M. Valldor, Synthesis and Characterization of Oxide Chloride Sr_2VO_3Cl, a Layered $S = 1$ Compound, *ACS Omega*, 2023, **8**, 14233–14239.

48 C. S. Knee, A. A. Zhukov and M. T. Weller, Crystal Structures and Magnetic Properties of the Manganese Oxide Chlorides Sr_2MnO_3Cl and $Sr_4Mn_3O_{8-y}Cl_2$, *Chem. Mater.*, 2002, **14**, 4249–4255.

49 A. L. Hector, J. A. Hutchings, R. L. Needs, M. F. Thomas and M. T. Weller, Structural and Mössbauer Study of Sr_2FeO_3X (X = F, Cl, Br) and the Magnetic Structure of Sr_2FeO_3F, *J. Mater. Chem.*, 2001, **11**, 527–532.

50 N. McGlothlin, D. Ho and R. J. Cava, $Sr_3Co_2O_5Cl_2$ and Sr_2CoO_3Cl: Two Layered Cobalt Oxychlorides, *Mater. Res. Bull.*, 2000, **35**, 1035–1043.

51 Y. Tsujimoto, K. Yamaura and T. Uchikoshi, Extended Ni(III) Oxyhalide Perovskite Derivatives: Sr_2NiO_3X (X = F, Cl), *Inorg. Chem.*, 2013, **52**, 10211–10216.

52 G. Tobías, D. Beltrán-Porter, O. I. Lebedev, G. V. Tendeloo, J. Rodríguez-Carvajal and A. Fuertes, Anion Ordering and Defect Structure in Ruddlesden–Popper Strontium Niobium Oxynitrides, *Inorg. Chem.*, 2004, **43**, 8010–8017.

53 J. R. Guarin, C. Frontera, J. Oro-Sole, B. Colombel, C. Ritter, F. Fauth, J. Fontcuberta and A. Fuertes, Anionic and Magnetic Ordering in Rare Earth Tantalum Oxynitrides with an $n = 1$ Ruddlesden–Popper Structure, *Chem. Mater.*, 2024, **36**, 5160–5171.

54 F. D. Romero, A. Leach, J. S. Möller, F. Foronda, S. J. Blundell and M. A. Hayward, Strontium Vanadium Oxide–Hydrides: "Square-Planar" Two-Electron Phases, *Angew. Chem., Int. Ed.*, 2014, **53**, 7556–7559.

55 C. Tassel, Y. Goto, D. Watabe, Y. Tang, H. Lu, Y. Kuno, F. Takeiri, T. Yamamoto, C. M. Brown, J. Hester, Y. Kobayashi and H. Kageyama, High-Pressure Synthesis of Manganese Oxyhydride with Partial Anion Order, *Angew. Chem., Int. Ed.*, 2014, **55**, 9667–9670.

56 M. A. Hayward, E. J. Cussen, J. B. Claridge, M. Bieringer, M. J. Rosseinsky, C. J. Kiely, S. J. Blundell, I. M. Marshall and F. L. Pratt, The Hydride Anion in an Extended Transition Metal Oxide Array: $LaSrCoO_3H_{0.7}$, *Science*, 2002, **295**, 1882–1884.

57 G. Kobayashi, Y. Hinuma, S. Matsuoka, A. Watanabe, M. Iqbal, M. Hirayama, M. Yonemura, T. Kamiyama, I. Tanaka and R. Kanno, Pure H^- conduction in oxyhydrides, *Science*, 2016, **351**, 1314–1317.

58 F. Takeiri, A. Watanabe, K. Okamoto, D. Bresser, S. Lyonnard, B. Frick, A. Ali, Y. Imai, M. Nishikawa, M. Yonemura, T. Saito, K. Ikeda, T. Otomo, T. Kamiyama, R. Kanno and G. Kobayashi, Hydride-ion-conducting K_2NiF_4-type Ba–Li oxyhydride solid electrolyte, *Nat. Mater.*, 2022, **21**, 325–330.

59 Y. Iwasaki, N. Matsui, K. Suzuki, Y. Hinuma, M. Yonemura, G. Kobayashi, M. Hirayama, I. Tanakadhij and R. Kanno, Synthesis, crystal structure, and ionic conductivity of hydride ion conducting Ln_2LiHO_3 (Ln = La, Pr, Nd) oxyhydrides, *J. Mater. Chem. A*, 2018, **6**, 23457–23463.

60 A. Fuertes, Prediction of Anion Distributions Using Pauling's Second Rule, *Inorg. Chem.*, 2006, **45**, 9640–9642.

61 M. L. Myrick, M. N. Simcock, M. Baranowski, H. Brooke, S. L. Morgan and J. N. McCutcheon, The Kubelka-Munk Diffuse Reflectance Formula Revisited, *Appl. Spectrosc. Rev.*, 2011, **46**, 140–165.

62 P. Makuła, M. Pacia and W. Macyk, How To Correctly Determine the Band Gap Energy of Modified Semiconductor Photocatalysts Based on UV-Vis Spectra, *J. Phys. Chem. Lett.*, 2018, **9**, 6814–6817.

63 F. A. Kröger and H. Vink, Relations Between the Concentrations of Imperfections in Crystalline Solids, *Solid State Phys.*, 1956, **3**, 307–435.

64 J. C. Li, L. Yang, J. G. Xu, A. J. Fernández-Carrión and X. J. Kuang, Tetrahedral Tilting and Oxygen Vacancy Stabilization and Migration in $La_{1-x}Sr_{2+x}(GaO_4)O_{1-0.5x}$ Mixed Electronic/Oxide Ionic Conductors, *Inorg. Chem.*, 2022, **61**, 5413–5424.

65 K. Fujii, Y. Esaki, K. Omoto, M. Yashima, A. Hoshikawa, T. Ishigaki and J. R. Hester, New Perovskite-Related Structure Family of Oxide-Ion Conducting Materials $NdBaInO_4$, *Chem. Mater.*, 2014, **26**, 2488–2491.

66 L. H. Li, M. Li, I. M. Reaney and D. C. Sinclair, Mixed ionic-electronic conduction in $K_{1/2}Bi_{1/2}TiO_3$, *J. Mater. Chem. C*, 2017, **5**, 6300–6310.

67 L. L. Wong, K. C. Phuah, R. Y. Dai, H. M. Chen, W. S. Chew and S. Adams, Bond Valence Pathway Analyzer-An Automatic Rapid Screening Tool for Fast Ion Conductors within softBV, *Chem. Mater.*, 2021, **33**, 625–641.

© 2025 The Author(s). Published by the Royal Society of Chemistry

Open Access Article. Published on 18 December 2024. Downloaded on 2/10/2026 7:04:31 AM.
This article is licensed under a Creative Commons Attribution-NonCommercial 3.0 Unported Licence.

68 H. Chen, L. L. Wong and S. Adams, SoftBV–A Software Tool for Screening the Materials Genome of Inorganic Fast Ion Conductors, *Acta Crystallogr., Sect. B:Struct. Sci., Cryst. Eng. Mater.*, 2019, **75**, 18–33.

69 W. Paulus, H. Schober, S. Eibl, M. Johnson, T. Berthier, O. Hernandez, M. Ceretti, M. Plazanet, K. Conder and C. Lamberti, Lattice Dynamics To Trigger Low Temperature Oxygen Mobility in Solid Oxide Ion Conductors, *J. Am. Chem. Soc.*, 2008, **130**, 16080–16085.

70 J. E. Auckett, A. J. Studer, E. Pellegrini, J. Ollivier, M. R. Johnson, H. Schober, W. Miiller and C. D. Ling, Combined Experimental and Computational Study of Oxide Ion Conduction Dynamics in $Sr_2Fe_2O_5$ Brownmillerite, *Chem. Mater.*, 2013, **25**, 3080–3087.

71 X. Y. Yang, A. Fernandez-Carrion and X. J. Kuang, Oxide Ion-Conducting Materials Containing Tetrahedral Moieties: Structures and Conduction Mechanisms, *Chem. Rev.*, 2023, **123**, 9356–9396.

72 F. Takeiri, A. Watanabe, A. Kuwabara, H. Nawaz, N. I. P. Ayu, M. Yonemura, R. Kanno and G. Kobayashi, Ba_2ScHO_3: H^- conductive layered oxyhydride with H^- site selectivity, *Inorg. Chem.*, 2019, **58**, 4431–4436.

73 H. Nawaz, F. Takeiri, A. Kuwabara, M. Yonemura and G. Kobayashi, Synthesis and H^- conductivity of a new oxyhydride Ba_2YHO_3 with anion-ordered rock-salt layers, *Chem. Commun.*, 2020, **56**, 10373–10376.